









RESEARCH ARTICLE | MARCH 05 2024

## Study of radiative shocks using 2D interferometry and XUV spectroscopy

R. L. Singh ; C. Stehlé ; M. Kozlova; M. Cotelo ; J. Dostal; R. Dudzák ; R. Rodriguez ; P. Velarde ; P. Barroso; F. Suzuki-Vidal ; T. Pisarczyk 



*Phys. Plasmas* 31, 033301 (2024)

<https://doi.org/10.1063/5.0188810>



View  
Online



Export  
Citation

CrossMark



### APL Machine Learning

2023 Papers with Best Practices in Data Sharing and Comprehensive Background

[Read Now](#)

# Study of radiative shocks using 2D interferometry and XUV spectroscopy

Cite as: Phys. Plasmas **31**, 033301 (2024); doi: 10.1063/5.0188810

Submitted: 24 November 2023 · Accepted: 2 February 2024 ·

Published Online: 5 March 2024



View Online



Export Citation



CrossMark

R. L. Singh,<sup>1,a)</sup> C. Stehlé,<sup>2</sup> M. Kozlova,<sup>1,3</sup> M. Cotelo,<sup>4</sup> J. Dostal,<sup>3,5</sup> R. Dudzák,<sup>3,5</sup> R. Rodriguez,<sup>6</sup> P. Velarde,<sup>4</sup> P. Barroso,<sup>7</sup> F. Suzuki-Vidal,<sup>8</sup> and T. Pisarczyk<sup>9</sup>

## AFFILIATIONS

<sup>1</sup>Extreme Light Infrastructure ERIC, ELI-Beamlines Facility, 25241 Dolní Břežany, Czech Republic

<sup>2</sup>LERMA, Sorbonne-Université, Observatoire de Paris, CNRS, 75014 Paris, France

<sup>3</sup>Institute of Plasma Physics, Czech Academy of Science, 18200 Prague, Czech Republic

<sup>4</sup>Instituto de Fusion Nuclear Guillermo Velarde, Universidad Politécnica de Madrid, José Gutiérrez Abascal 2, 28006 Madrid, Spain

<sup>5</sup>Institute of Physics of the Czech Academy of Sciences, Na Slovance 1999/2, 182 21 Prague, Czech Republic

<sup>6</sup>Universidad de Las Palmas de Gran Canaria, 35001 Las Palmas, Spain

<sup>7</sup>GEPI, Observatoire de Paris, Université PSL, CNRS, Place Jules Janssen, F-92195 Meudon, France

<sup>8</sup>First Light Fusion Ltd., OX5 1QU Oxford, United Kingdom

<sup>9</sup>The Institute of Plasma Physics and Laser Microfusion, 01-497 Warsaw, Poland

<sup>a)</sup> Author to whom correspondence should be addressed: [raj.laxmisingh@eli-beams.eu](mailto:raj.laxmisingh@eli-beams.eu) and [raaj.phys@gmail.com](mailto:raaj.phys@gmail.com)

## ABSTRACT

We report new experimental results on radiative shocks obtained in Xenon and Argon in gas cells at two different pressures below 1 bar. These shock waves are generated by the interaction of the PALS iodine laser on a CH–Au foil with a typical velocity in the range of 50–100 km/s depending on the variable laser intensity, pressure, and gas. Attention is paid to the morphology and the dynamics of the radiative precursor over large time scales up to 30 ns, using 2D sub-picosecond visible interferometry, illustrating the complex interplay of hydrodynamic and radiation absorption for different initial conditions. The comparison between 1D and 2D simulations confirms the role played by lateral radiative losses in the ionization wave and the necessity of state-of-the-art integrated opacities. This study is complemented by the first XUV analysis of the shock emission between 5 and 20 nm obtained with a grating spectrometer, with line identification, which is compatible with the ionization stages deduced from interferometry and simulations.

Published under an exclusive license by AIP Publishing. <https://doi.org/10.1063/5.0188810>

## I. INTRODUCTION

With the avenue of high-energy and high-intensity lasers, it is possible to study shock waves on Earth in different ways, which have a link with those that are present in space. The shock regime depends on the shock velocity, density, and temperature of the initial and shocked plasma and can thus be collisional or not, magnetized or not.

Collisionless shocks abound in the Universe and are widely studied from the non-relativistic to the relativistic case.<sup>1–3</sup> They are, in particular, supposed to be the source of high-energy cosmic rays in high-energy astrophysical environments and under various effects involving for instance turbulence and magnetic fields.<sup>4</sup> As a consequence of the propagation of these accelerated charged particles, such shocks may generate a precursor ahead of the shock. Collisionless shocks are also studied in the laboratory in the relativistic and non-relativistic regimes.<sup>5–7</sup>

Collisional shocks occur in dense plasmas.<sup>8,9</sup> At large shock velocities, the post-shock is heated and thus radiates. Within the radiative shock regime, there are two additional sub-classes, depending on the shock generation. In the case of an instantaneous point source explosion in a low-density medium, the spherical blast wave regime prevails.<sup>10</sup> Alternatively, the shock may be sustained at longer times by a driving piston.<sup>11</sup>

Shock waves may be the host of various instabilities. In the case of non-magnetized collisional plasma, they can be either hydrodynamical<sup>12</sup> or radiative as in the case of the thermal cooling instability,<sup>13</sup> which is observed in stellar accretion shocks. Radiative instabilities have also been already experimentally observed in the post-shock of an expanding shock wave<sup>10,14</sup> and should develop in a specific range of plasma temperature and density conditions.<sup>15</sup>

Radiative shocks occur thus at large velocities (compared to the sound velocity) such that high temperatures are obtained in the compressed matter.<sup>16</sup> They are characterized by a strong coupling between hydrodynamics and radiation.<sup>9</sup> At low densities, the radiation, which escapes from the structure, acts as a cooling mechanism. At higher densities, this radiation emitted by the hot post-shock may be partly absorbed, particularly by the colder gas in which the shock propagates. This leads to the development of the radiative precursor preceding the density discontinuity. Such precursors are visible in various circumstances, for instance, the top of high velocity (several 100 km/s) stellar jets propagating in the interstellar medium,<sup>17</sup> in the case of accretion shocks,<sup>18–20</sup> or when the shocks emerge from the atmosphere of exploding supernovae.<sup>21,22</sup>

Radiative shocks have been the objects of many theoretical works.<sup>9,23–26</sup> They are considered as a test case of coupling between radiation and hydrodynamic,<sup>27–30</sup> which in turn need to be tested against dedicated experiments. In addition to a few experiments performed on electric pulsed power installations,<sup>31–33</sup> the majority of the experiments have been performed on high energy nanosecond laser installations,<sup>11,34–42</sup> with laser intensity on the target of about  $10^{14}$  W/cm<sup>2</sup>. As radiative effects increase with the Mach number, most experiments have been performed in heavy gases like Xenon, at various initial pressures, where typical shock velocities are in the range of 50 km/s and are analyzed over a few nanoseconds.

As a consequence of a large number of ionization stages and excitation levels, the strong shocks in heavy gases are characterized by a high post-shock compression,<sup>16</sup> which may exceed ten compared to the adiabatic gas compression of four. Thus, the shock velocity remains closer to the piston velocity. This effect is reinforced by radiation cooling.<sup>35</sup> In addition to this, the most important signature of these shocks is the development of a radiative precursor ahead of the shock front, which is the consequence of the radiation absorption during its transfer in the unshocked gas.

Numerical simulations of these phenomena have often been performed using 1D radiative hydrodynamical simulations.<sup>11,43</sup> If such simulations present the interest to provide useful indications about the plasma conditions, however, as shown earlier, to compare more precisely with the experiments, 2D simulations are necessary, even if the plasma is confined within the target boundaries.<sup>29,30,36,38</sup> All these simulations are strongly dependent on the quality of the Planck and Rosseland averaged opacities.<sup>15</sup>

A complete view of these shocks would require an image of both the thin post-shock layer and the more extended radiative precursor. The best candidate for this is the combination of XUV (Extreme Ultraviolet) imaging, which allowed us to visualize both the post-shock and the high-density region of the precursor.<sup>38</sup> If few experiments were able to show the development of instabilities in the post-shock region through high-resolution x-ray imaging,<sup>39</sup> most experiments concentrated on the radiative precursor<sup>36,44</sup> using visible techniques. However, there is a lack of systematic study of the effect of the initial pressure, gas nature, and laser intensity on the target, which is one of the objectives of the present study, using time-resolved visible interferometry. This diagnostic enables us to visualize for the various conditions (nature of the gas, pressure, focal spot, and laser energy) the space and time evolution of the radiative precursor, through the measurement of its electron density.

Interestingly, although shock spectroscopic signatures are widely used in astrophysics, their study remains experimentally poor for

shocks generated by lasers.<sup>36,40</sup> However, as in astrophysics, they could be indicators of the shock velocity by the Doppler effect of the plasma temperature. Whereas radiative transfer in the lines has often been taken into account for interpreting many astronomical observations; this last aspect is today not taken into account experimentally due to the challenge in spectroscopic detection. To increase the bridge with astrophysical shocks, it is now necessary to complete these experimental works with the analysis of their spectroscopic signatures. This aspect remains today challenging and has never been touched on in detail. A first step in this direction will be proposed in the present work.

In this context, our work concerns a comparative study of laser-generated shock waves obtained at the PALS laser facility, with a focus on the radiation effects on the shock topology, dynamics, and their signatures for two different noble gases (Argon and Xenon) at two different pressures and for different laser conditions. Several questions motivate this study: Is the precursor development faster for the lighter gas? For a lower pressure? Is the ionization wave monotonically decreasing with time? What is the influence of the diameter of the laser focal spot? What is the effect of the walls? What are the influences of opacity on the dynamics and topology and dynamics of the precursor for the same initial laser conditions? What are the expected spectral signatures of the shock? Is it possible to obtain detailed spectroscopic data?

The paper is structured as follows: Sec. II provides a detailed discussion on the experimental setup, while the interferometric results are presented in Sec. III. Section IV delves into the modeling of the shock wave, and Sec. V is dedicated to the analysis of experimental XUV spectra. The paper concludes with Sec. VI, where we present a summary of our findings and draw meaningful conclusions.

## II. EXPERIMENTAL SETUP

The experiment was performed at the kJ PALS iodine laser facility.<sup>45</sup> An overall layout of the experiment is presented in Fig. 1. The 4 mm long parallelepipedic gas cell target is closed by a coated CH foil at one end and by a brass disk on the opposite side. The Au-CH foil acts as a piston to launch the shock. The target cells were filled with

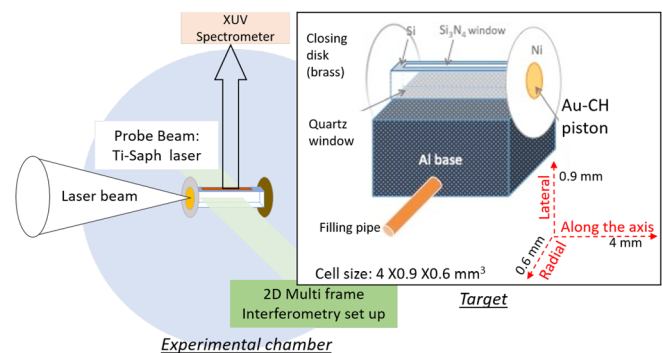


**FIG. 1.** Layout of the experimental setup and target (in the inset). The laser beam (0.3 ns, 100–180 J, 430 nm) focuses on the CH layer of the Au-CH piston of the target. An XUV spectrometer looks from the top through the SiN window of the target. The direction of the Ti-Saph probe beam for the 2D interferometry is presented in the schematic in green color. It propagates through the two lateral quartz windows.

noble gases [Xe, Xe+He (90–10% mixture) or Ar at a pressure between 0.2 and 0.6 bar].

The laser (438 nm, 0.35 ns) with energy 100–180 J at  $3\omega$  was focused on the Au–CH foil of the target with a focus size of about 250–350  $\mu\text{m}$ . The typical laser peak intensity is  $\sim 4 \times 10^{14} \text{ W/cm}^2$  for a 350  $\mu\text{m}$  focal spot and energy 145 J.

Due to the incidence of the laser on the Au–CH foil, the shock was launched and propagated in the gas cell toward the closing disk. This shock propagation was recorded using visible interferometry and XUV spectroscopy. The CH (Parylene-N; 10  $\mu\text{m}$ ) foil was used as an ablator during the laser–matter interaction, and the thin layer of Au (580 nm) was placed on the side of the interior of the tube, aiming at preventing x-ray radiation. The top window of the target was made of a 100 nm thick  $\text{Si}_3\text{N}_4$  window supported by a 0.2 mm thick Si frame to pass the shock XUV radiation toward the XUV spectrometer. The two lateral windows, separated by a distance of 0.6 mm, were made of 0.5 mm thick quartz with anti-reflective visible coating and were thus adapted to the visible interferometric diagnostic (see Fig. 1). The details of these diagnostics setups are presented in the following sections.

As indicated previously, two different noble gases (Xe and Ar) were studied to inspect the variation of the radiative shock (speed and structure) vs the atomic number: pure Xenon, a mixture of XeHe (90/10% in the number of atoms), and Argon. The inclusion of a small proportion of Helium was chosen for comparison with an earlier study,<sup>40</sup> showing that the presence of the lines of  $\text{He}^+$  is a complementary indicator of the plasma temperature. This small quantity of Helium affects marginally the shock dynamics compared to the case for pure Xenon. The gas pressure varied between 0.2 and 0.6 bar.

Throughout the experimental campaign, multiple shots were conducted, varying parameters such as gas type (XeHe or Ar), initial gas pressure, laser energy, and spot size. In this paper, we focus on presenting results from a selected subset of shots, which are detailed in Table I.

### A. Visible interferometry

A Ti: Saph laser (wavelength: 811 nm, diameter: 30 mm, energy < 1 mJ, and pulse duration > 40 fs) was used in the visible interferometry imaging setup. This laser was synchronized with the PALS beam.<sup>46</sup>

The probing laser was separated into three independent beams in the vertical plane, with different angles between them, spaced by  $3^\circ$ . With this setup, we could record the images between 3 and 30 ns with its initial time  $t_0$  (launch of the shock). An optical delay is

TABLE I. All the shots discussed in this paper are listed in this table.

Shot Number	Focal spot ( $\mu\text{m}$ )	Gas	Gas pressure P (bar)	Laser energy E (Jule)
50 363	350	XeHe	0.6	95
50 364	350	XeHe	0.6	170
50 365	350	XeHe	0.6	144
50 373	350	Ar	0.6	184
50 381	350	Ar	0.2	111
50 391	350	Ar	0.2	168
50 387	280	Xe	0.6	103
50 389	280	Ar	0.6	134

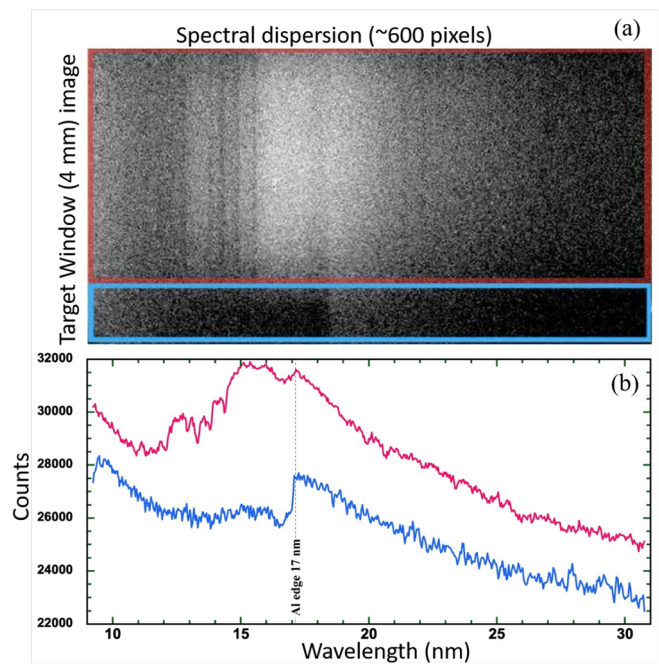


FIG. 2. (a) The raw XUV spectral image for shot 50389 in Argon is displayed, with two highlighted rectangles in red and blue. The red rectangle represents emission from the uncovered portion of the target, while the blue rectangle corresponds to the part covered by the Al filter. (b) Integrated spectral profiles in red and blue correspond to the red and blue rectangular areas marked in panel (a), respectively.

implemented between these three interferometric arms to provide images of the moving shock at three times separated by 12 ns. Each interferometer is based on the half Fresnel bi-prism (a layout of this setup is presented in Fig. 2 of Kasperczuk and Pisarczyk<sup>47</sup>), and the record is made on three CCD cameras ( $2048 \times 2048$  pixels, pixel size  $7.4 \times 7.4 \mu\text{m}$ ; 16 bits dynamics) placed at 2 m from the vacuum chamber. The magnification of the setup is two.

### B. XUV spectroscopy

The time and space integrated XUV emission spectra between 10 and 35 nm have been recorded, employing a flat field XUV spectrometer using a concave gold coated VLS (Variable Line Spacing) grating (curvature radius of 5649 mm, 1200 grooves per mm, efficient grating area of  $45 \times 27 \text{ mm}$ , and blaze angle  $3.7^\circ$ ). For the detector, an image plate (BAS-IP TR 2040) is placed at a distance of  $\sim 240 \text{ mm}$  from the grating, which is itself located at a distance of  $\sim 320 \text{ mm}$  from the target. IP detectors have an advantage (over the CCD) to be less sensitive to the harsh environment EMP (Electromagnetic Pulse) and can be used without the protecting film. The spectrometer was installed on top of the vacuum chamber (Fig. 1).

An Al filter (0.8  $\mu\text{m}$ ) covers part of the nose of the spectrometer corresponding to the field of view of the back side of the shock tube. It provides a useful reference wavelength (sharp edge at 17–17.1 nm, Fig. 2) in the spectrum. This choice allows monitoring on the Image Plate both the spectrum of the shock without the Al filter (part of the target close to the laser impact) and with this filter (back side of the target). It should be noted that the  $\text{Si}_3\text{N}_4$  window introduces a smoother

edge near 12.4 nm.<sup>48</sup> There is no additive angular limitation than the section of the XUV windows of the targets.

### III. INTERFEROMETRIC RESULTS

For a given gas, low pressures are more favorable to the development of an extended but weaker radiative precursor (due to a reduced absorption), and high pressures are more favorable for the XUV spectroscopic analysis, which requires a sufficient number of emitting ions. On the other hand, for the same pressure, the shock velocity should reduce when increasing either the atomic mass (i.e., passing from Argon to Xenon) or increasing the pressure. However, the shock velocity is mostly given by the speed of the laser-driven piston, and thus the mass effect remains marginal compared with the velocity of the ionization wave (precursor).

In Sec. III A, we will present the general topology (geometry, extension) of the radiative precursor for two different laser spot sizes. The interferometric records will provide the electron density and the precursor velocity for different pressures, laser energies, and focal spots. These results will then be compared with numerical simulations.

#### A. A typical topology of the interferometric images

Typical interferometric records for the single shot 50365 with XeHe gas at 0.6 bar and laser energy 144 J (focal spot of  $\sim 330 \pm 30 \mu\text{m}$ , thus, intensity  $\sim 4.3 \times 10^{14} \text{ W/cm}^2$ ) are presented for three different times (5, 17, and 29 ns after shock launching) in Fig. 3. The laser comes from the left at time 0 and the shock propagates from the left to the right of the tube. For this shot, a quartz obstacle was placed in the right part of the channel. The objective of this obstacle was to check the potential preheating of the quartz windows at distances from the shock. Indeed, a similar experiment has been performed at higher laser intensities and shock velocities showing some preheating of the obstacle.<sup>49</sup> Dark zones may be noticed in the records, before and after the shot. They are associated with irregular traces of glue on the upper part of the channel and between  $\sim 2000$  and  $3000 \mu\text{m}$ , on the quartz obstacle itself. The sharp interferograms trace the low-density radiative precursor, whereas the denser post-shock (on the left) is opaque to the light of the Ti-Saph laser.

At large densities, the interval between the fringes reduces and the fringes are narrower. In addition, we note that these fringes, which are still visible in the middle of the channel, become less and less visible laterally when the density increases. This effect, which is present in all the shots, could be attributed to residual parasitic diffraction patterns, which superpose to the signal and make it difficult to distinguish from the background. Another explanation could be linked to the slip in the time overlap between the probe and reference beams. Hence, contrarily to the reference beam, the probe beam is deflected by the change of the refractive index in the zones where the plasma is dense and bent. To illustrate this, let us take the ideal case of a uniform cylindrical plasma at a constant electron density inside the channel. The probe laser beam passing through this plasma is deflected two times (at the entrance and the exit of the plasma). For a density of  $7 \times 10^{19} \text{ cm}^{-3}$  (resp  $10^{20} \text{ cm}^{-3}$ ), this induces a net delay on a detector (placed at  $\sim 2.5 \text{ m}$  from the tube), which is sufficient to loosen the fringes over 10% (resp 30%); see Fig. 4.

The line-integrated electron density ( $\langle N_e \rangle$ ) was deduced by measuring the fringe shift, employing the formulas outlined in Eqs. (1) and (2) from Singh *et al.*<sup>40</sup> This measurement involved comparing the

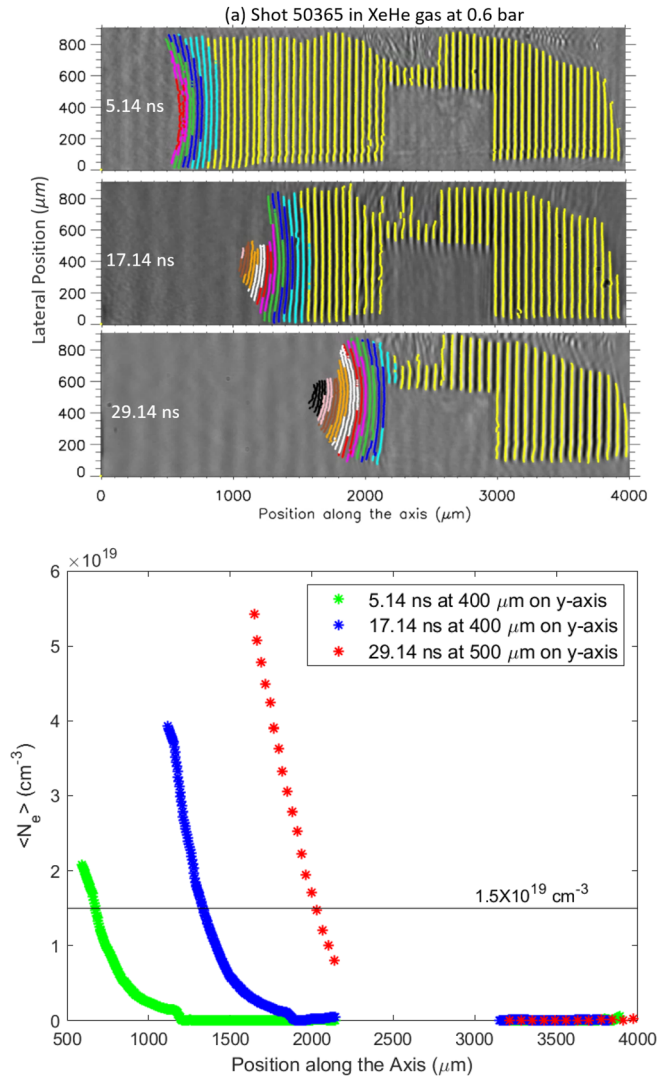


**FIG. 3.** (a) Recorded 2D shock interferometric images at 5, 17, 29 ns for shot 50365 in XeHe, at 0.6 bar. The laser energy is 144 J, with a focal spot diameter of  $350 \mu\text{m}$ . Traces of glue are visible on the top face of the channel, between  $\sim 2100$  and  $2800 \mu\text{m}$ . (b) The line-integrated electron density ( $\langle N_e \rangle$ ) profiles for the interferometric images are presented at the top. These profiles are plotted at the symmetry axis of the precursor along  $y$ . There is no record of the position of the obstacle located between  $2350$  and  $3150 \mu\text{m}$ . A horizontal line at  $1.5 \times 10^{19} \text{ cm}^{-3}$  serves as a reference marker in the plot for velocity determination corresponding to Fig. 6 and Table III.

shocked image captured during the shot with the reference image recorded before the shot. A more detailed method can be seen in Singh *et al.*<sup>40</sup> The uncertainty would be linked to the determination of the position of the fringe maxima (which is 1 pixel  $\sim 3.8 \mu\text{m}$ ). The fringe width decreases from low density to high density. For example, for the interferogram of shot 50365 (Fig. 3 in the paper) at 5.14 ns, the fringe width (FWHM) varies from 26 (at  $\langle N_e \rangle = 2.1 \times 10^{19} \text{ cm}^{-3}$ ) to 11 s (at  $\langle N_e \rangle = 5 \times 10^{17} \text{ cm}^{-3}$ ). Therefore, the fringe width is always larger than 3 pixels. Taking 2 pixels for the precision of the sampling, this

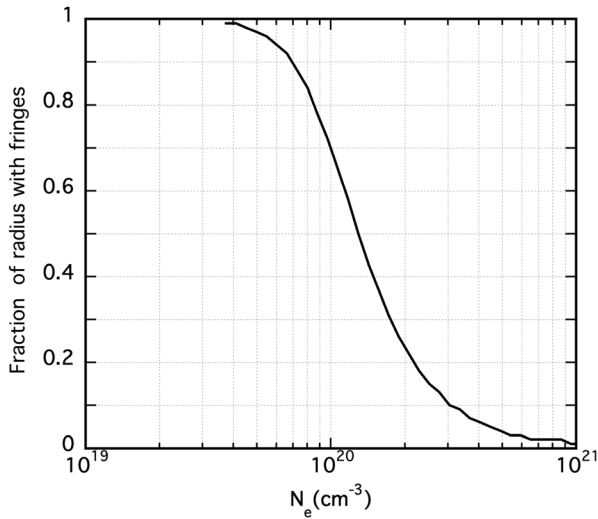


**FIG. 4.** Fraction of a plasma tube at a uniform electron density  $N_e$ , which is covered by fringes. The detector is placed at a distance  $L = 2.5$  m from the plasma cylinder and for the duration of the probing laser pulse is set to 40 fs.

gives the position a precision of  $\sim 7 \mu\text{m}$ , which gives for the evaluation of the velocity (presented in Fig. 6) for a time interval equal to 4 ns less than 2 km/s and 0.6 km/s for a time interval equal to 12 ns.

To highlight the variation in electron density with the position, we divided electron density into 13 bins, each of them having a specific color, as indicated in Table II. The measured maximum electron density increases with time from  $\sim 2 \times 10^{19} \text{ cm}^{-3}$  at 5.14 ns up to about  $\sim 6 \times 10^{19} \text{ cm}^{-3}$  at 29.14 ns.

The precursor develops longitudinally with time. It first extends rapidly. Then, it slows slightly down with time, as can be seen from the longitudinal profiles of  $\langle N_e \rangle$  in Fig. 3 (bottom panel) plotted at the “symmetry” axis of the precursor along  $y$  (which may slightly differ

**TABLE II.** Division of the averaged electron density into thirteen bins and their color representation.

Electron density range $\langle N_e \rangle$ ( $\text{cm}^{-3} \times 10^{19}$ )	Color
0–0.38	Yellow
0.38–0.75	Cyan
0.75–1.13	Blue
1.13–1.51	Lime green
1.51–1.89	Magenta
1.89–2.26	Red
2.26–3.01	White
3.01–3.76	Orange
3.76–4.52	Brown
4.52–5.27	Pink
5.27–7.53	Black
7.53–11.3	Steel blue
11.3–15.1	Sea green

from the axis of symmetry of the channel). Here, the symmetry axes of precursors recorded at 5, 17, and 29 ns are, respectively, set to 400, 400, and 500  $\mu\text{m}$ .

At high densities, the plasma becomes more opaque and the contrast of the fringe decreases. They also become very thin and closer to each other. The maximum line integrated electron density,  $\sim 6 \times 10^{19} \text{ cm}^{-3}$ , is about 1/30 of the critical density. Due to the increasing opacity and the confusion in the fringes, it remains difficult to visualize higher electron densities.

In the present example, the radiative shock is unaffected by the obstacle up to 17 ns. Up to 18 ns, the fringes and the obstacle itself remain unperturbed before the obstacle; thus, there is no evidence of any preheating linked to this quartz obstacle at the distance of the precursor induced by high-energy radiation. At 29 ns, the radiative precursor is close to the obstacle and is impacted by it for the low-density part. The obstacle itself seems to be unaffected at this time. The following records presented in this study will be performed without any obstacle and will assume the absence of any preheating of quartz windows of the tube ahead of the shock front.

Our interferometric images allow us to measure the speed of radiative heating. This last quantity depends on the value of the average electron density  $\langle N_e \rangle$ . As long as the precursor extends with time, the lower values of  $\langle N_e \rangle$  have a larger velocity than the higher values, which are closer to the shock front. For instance, in this record, we deduced velocities at 4, 16, and 29 ns of about 131 km/s (at the launching phase), 78, and 70 km/s stabilization phases, respectively, for the isocontour  $\langle N_e \rangle \sim 1.5 \times 10^{19} \text{ cm}^{-3}$  in Fig. 3(b).

### B. Effect of the tight focus

Most of the shots were performed for a focal spot of about 350  $\mu\text{m}$  diameter. However, for Xenon at 0.6 bar, we studied the impact of the focal spot diameter variation on the target. This is obtained through the displacement of the focal lens of the laser. In Fig. 5, we present typical single-shot 50 387 results with laser energy 103 J for Xe gas at 0.6 bar. From the keV camera, the focal spot diameter is then estimated at  $\sim 280 \pm 30 \mu\text{m}$  and the intensity is of the order of  $4.8 \times 10^{14} \text{ W/cm}^2$ , which is comparable to the conditions of the previous shot 50 365 (Fig. 3). The 2D interferometric images were recorded at 4, 16, and 28 ns. Except for the first snapshot at 4 ns, where the bending of the fringes is more pronounced than in the previous record at 5 ns, and the velocity is higher, the global behavior of the precursor at later times is globally similar to the previous one: the radiation flux coming from the shock reaches all the gas inside the channel and the precursor expands laterally. However, the initial value of the shock velocities for shot 50 387 is higher than previously at the short times and then presents a constant deceleration with the time. The deduced velocities (Fig. 5) at 4, 16, and 28 ns are about 169, 73, and 39 km/s, respectively for the isocontour  $\langle N_e \rangle \sim 1.5 \times 10^{19} \text{ cm}^{-3}$  at the symmetry axis of the precursor.

### C. Variations with the atomic mass, pressure, laser energy, and intensity

To investigate the effects of the pressure and the laser intensity, we will first compare in this section five records obtained at different laser energies but for the same spot diameter fixed to  $\sim 350 \mu\text{m}$ . To illustrate the effect of the tight binding, we shall in addition also

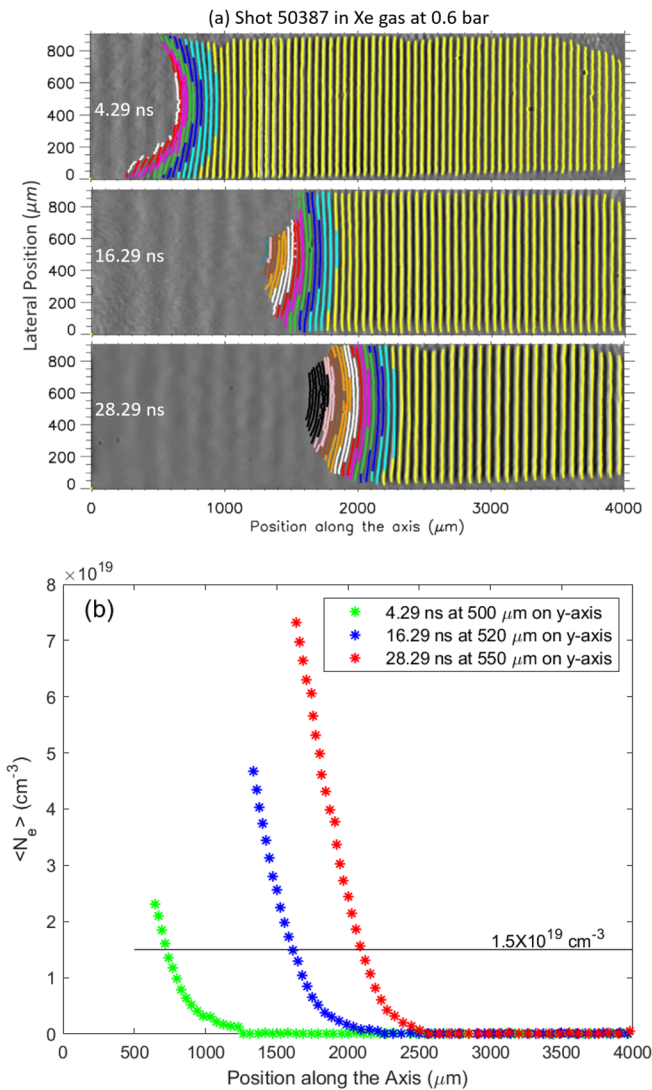


**FIG. 5.** (a) 2D shock interferometric images at 4, 16, 28 ns for shot 50387 in XeHe, at 0.6 bar. The laser energy for this shot is 103 J, and the focal spot is 280  $\mu\text{m}$ . (b) The line integrated electron density ( $\langle N_e \rangle$ ) profiles for the interferometric images presented on the top. These profiles are plotted at the symmetry axis of the precursor along y. A horizontal line at  $1.5 \times 10^{19} \text{ cm}^{-3}$  is shown in the plot as a marker for the velocity determination (corresponds to velocities shown in Fig. 6 and Table III).

present two shots at 0.6 bar obtained in the tight focus condition (i.e., focal spot  $\sim 280 \mu\text{m}$ ). The corresponding conditions of the records are summarized in Table III.

All the interferograms present a similar topology to the previous records (Figs. 3 and 5), with a smooth bending of the fringes, and a maximum electron density smaller than  $7 \times 10^{19} \text{ cm}^{-3}$  (black color), except for the shot 50389 [Fig. 14(b) and Table III] in Argon at 0.2 bar in the tight focus (and large laser energy) condition. For this later shot, the fringe pattern remains smooth for densities larger than  $10^{19} \text{ cm}^{-3}$  (red color). However, below this density, one notes a pre-ionization under the form of a spike at 4.4 ns (due to an identified tiny

defect in the gold coating of the piston foil), those extension reduces then with time. This shot is also unique to present fringes at densities larger than  $7.4 \times 10^{19} \text{ cm}^{-3}$ . The corresponding Fig. 14(b) is presented in the Appendix together with an example of a typical shot in Argon at 0.2 bar.

Comparing Argon at 0.6 bar (shot 50373 at 184 J) and Xenon at 0.6 bar (shot 50364 at 170 J) (see Table III), with the same focal spot of 350  $\mu\text{m}$ , we note a faster development in the case of Argon (velocity of  $\sim 85$  vs 60 km/s for Xenon). This may be attributed to a slightly larger laser energy inducing a higher velocity of the shock front. However, a more plausible interpretation is that for similar laser energy, the contribution of the gas opacity, which blocks the XUV radiation coming from the shock and which heats the cold gas, has to be taken into account. The monochromatic opacity of the cold gas being larger for Xenon, the heating wave will be slower for Argon than for Xenon.

Figure 6(a) presents the time variations of the velocity of the density isocontour equal to  $1.5 \times 10^{19} \text{ cm}^{-3}$  for the highest pressure

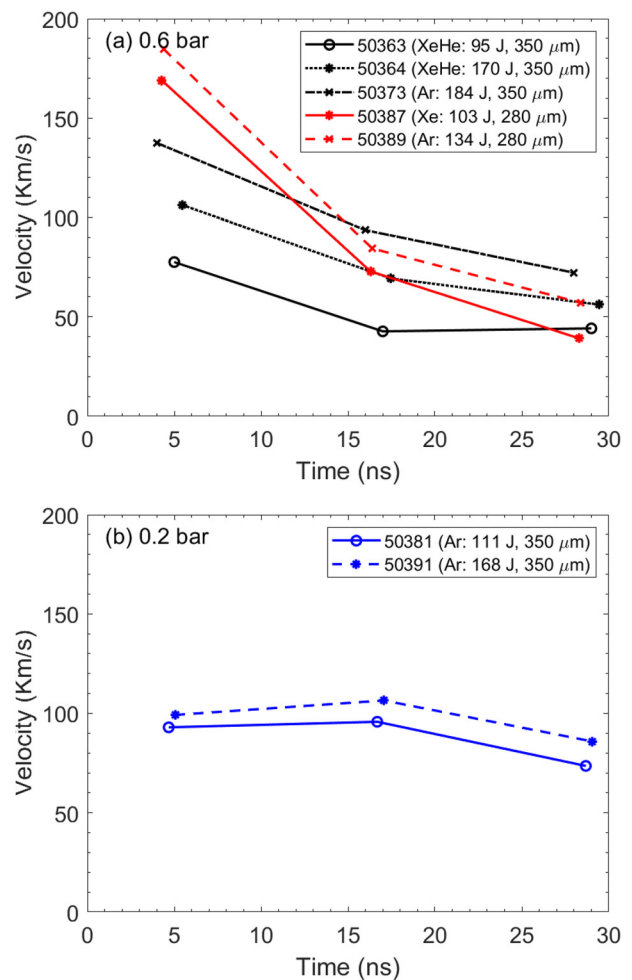


**FIG. 6.** Velocities of isocontours  $1.5 \times 10^{19} \text{ cm}^{-3}$  at 0.6 bar (a) and  $0.5 \times 10^{19} \text{ cm}^{-3}$  at 0.2 bar (b) at three different times for selected Xe, XeHe, and Ar shots. All the shots were performed with focal spot  $\sim 350 \mu\text{m}$  except shots 50387 and 50389 ( $\sim 280 \mu\text{m}$ , tight focus, in red color).

**TABLE III.** Velocity  $V$  in km/s at the latest time in ns for five different shots without any obstacle in the tube. Initial conditions: pressure  $P$  (bar), gas nature, mass density  $\rho$  ( $10^{-3} \text{ g cm}^{-3}$ ), ion density  $N_i$  ( $10^{19} \text{ cm}^{-3}$ ), laser Energy  $E$  (J), the electron density of the probed isocontour  $N_e$  ( $10^{19} \text{ cm}^{-3}$ ). The focal spot ( $\mu\text{m}$ ) of the laser is identical ( $\sim 350 \mu\text{m}$ ) in these shots except the two last shots 50 387 and 50 389 ( $\sim 280 \mu\text{m}$ , tight focus) in italic.

Shot	Focal spot	P	Gas	$\rho$	$N_i$	E	Time	$N_e$	V
50 363	350	0.6	XeHe	3	1.5	95	29	1.5	44
50 364	350	0.6	XeHe	3	1.5	170	29.46	1.5	56
50 373	350	0.6	Ar	1	1.5	184	28	1.5	88
50 381	350	0.2	Ar	0.3	0.5	111	28.68	0.5	75
50 391	350	0.2	Ar	0.3	0.5	168	29.06	0.5	103
50 387	280	0.6	Xe	3	1.5	103	28.29	1.5	39
50 389	280	0.6	Ar	1	1.5	134	28.4	1.5	57

(0.6 bar) for Argon and Xenon. Contrary to the post-shock, the precursor is only radiatively heated and is not compressed. Thus, this selected value corresponds to a small ionization stage equal to unity. As expected, for all the cases, the precursor develops more rapidly at the highest energy (both in position and extension).

Examining the impact of the initial gas pressure, a comparison between two Argon shots, 50 373 at 0.6 bar and 50 391 at 0.2 bar, reveals interesting dynamics. In the case of Argon at the lowest density of 0.2 bar in Fig. 6(b), contrarily to the previous cases shown in Fig. 6(a), the velocity stagnates or even increases slightly up to 15 ns, and decreases after this time. To analyze this behavior at 0.2 bar, we considered the isocontour at  $0.5 \times 10^{19} \text{ cm}^{-3}$  to maintain the ion stage equal to unity for comparison with results in Fig. 6(a). We attribute the slow radiative ionization during the initial times to the lower pressure and thus lower opacity. Consequently, due to the lower radiative heating efficiency, more time is required to ionize the gas. This qualitative explanation clarifies why the precursor remains less ionized than at 0.6 bar during the initial time (up to 5 ns). However, later on, the opacity increases with the temperature (Fig. 7) and this gradual increment allows a more pronounced ionization, and finally leads with the time to a behavior of the shock wave that matches the patterns observed in other cases.

The previous discussion was dedicated to comparing shots in Xenon and Argon with the largest focal spot ( $\sim 350 \mu\text{m}$ ), and we shall continue the analysis with the case of the tight focus described by shots 50 387 (Fig. 5) in Xenon and 50 389 [Fig. 14(b)] in Argon. Hence, the interferometric results, as illustrated in Fig. 6 and summarized in Table III, provide insights into key aspects such as the influence of varying laser spot diameters, precursor development in heavier vs lighter gas, and precursor development at different initial gas pressures. A comparative analysis of shots 50 387 (280  $\mu\text{m}$ , 0.6 bar Xe, 103 J) and 50 363 (350  $\mu\text{m}$ , 0.6 bar Xe, 95 J) shows the impact of spot diameter variation. Notably, for the smaller spot diameter in shot 50 387, the precursor velocity is significantly higher (approximately 170 km/s). However, due to lateral expansion, the velocity decreases more rapidly in this case of the tight, reaching 39 km/s at the last instant, in contrast to 44 km/s for shot 50 363.

A similar trend is observed in the comparison of two Argon shots at 0.6 bar, namely, shots 50 389 (280  $\mu\text{m}$ ) and 50 373 (350  $\mu\text{m}$ ). In two

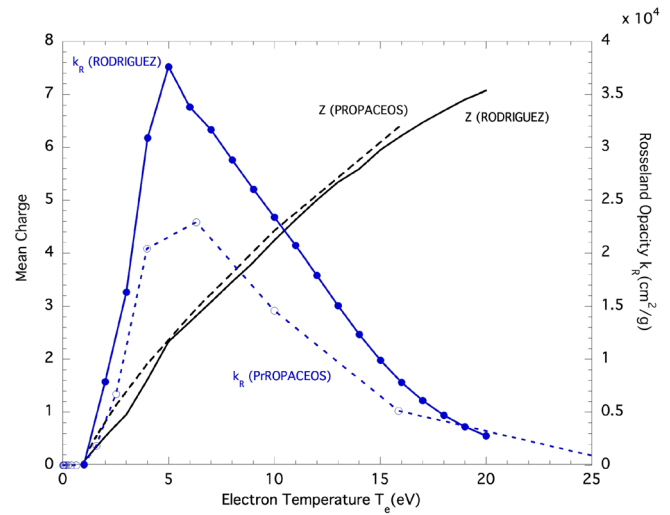


**FIG. 7.** Variations with the temperature of the Rosseland opacity  $k_R$  (in blue) and mean charge  $Z$  (in black) for Argon computed with the PROPACEOS (dashed line) and RODRIGUEZ (solid line) line models. The density of Argon is set to  $0.001 \text{ g cm}^{-3}$ .

distinct sets of shots (Set 1: 50 364, 50 373, and Set 2: 50 381, 50 363), the precursor development is consistently faster in lighter gas.

The summary of the estimation of the velocity at the latest time  $\sim 30$  ns is presented in Table III for the case of a 350 s focal spot, for different gases, laser energy, and pressure. The results show again that for the same gas and at the same pressure, the velocity increases with laser energy and decreases with the pressure. They also confirm that at constant pressure, the ionization velocity decreases with increasing atomic mass.

The previous interferometric results provide thus together information about the precursor's average electron density and its velocity. They also confirm the bent shape of the precursor obtained in previous studies, which is a consequence of the lateral radiative losses of the shock wave. The observed electron density reaches thus values close to  $1 \times 10^{18} \text{ cm}^{-3}$  (Figs. 3 and 5), but the position of the shock front, the density just before and after this front are unknown. Concerning the dynamics, taking the values at  $1.5 \times 10^{19} \text{ cm}^{-3}$  in the precursor, the velocity of the ionization wave is comprised of between 40 and 90 km/s depending on the case (see Table III). This gives an upper limit to the velocity of the shock front. However, this last one is not known. A complementary numerical analysis is then needed to complete the comprehension of the shock physics and propagation and will be the subject of the following Sec. IV. This study will precise the ionic stages that are expected to be observed by the XUV diagnostic and analyzed in Sec. V B.

#### IV. NUMERICAL MODELING OF THE SHOCK STRUCTURE AND DYNAMICS

This section then starts with a simple 1D description, using the Lagrangian radiative hydrocode HELIOS.<sup>50</sup> This will give a first qualitative comprehensive view of the physics at play, in terms of dynamics, opacity, and ionization for shock waves in Xenon and Argon. To perform a more quantitative comparison with the experiment, a 2D



analysis of the shock wave will be performed in conditions that are close to the experiment, both for Xenon and Argon. This will be done with the 2D adaptative mesh refinement (AMR) radiative hydrocode ARWEN code.

**A. A qualitative analysis with HELIOS 1D**

1D radiative hydrodynamic simulations are then useful at first glance to get fast and qualitative information about the shock structure: the existence of a precursor, compression, typical electron density, etc. Such simulations have been performed with the HELIOS software and associated PROPACEOS opacities and equation of state.<sup>50</sup>

We present in Fig. 7 the variations of the Rosseland opacities and the mean charge for Argon at a density of  $0.001 \text{ g cm}^{-3}$  vs temperature in eV for the PROPACEOS model and the model computed following the method described for Xenon in Rodriguez *et al.*<sup>15</sup> In these two calculations, LTE (Local Thermodynamic Equilibrium) approximation was assumed, which means that the populations of each ion were computed within the Saha-Boltzmann approximation. Hence, a detailed analysis of the validity of this thermodynamic regime has been performed in Rodriguez *et al.*<sup>15</sup> by comparing these results with those obtained from the solution of a set of coupled collisional-radiative equations, which include the transition rates among the atomic levels due to collisions with electrons and photons, which corresponds to the NLTE (Non-local thermodynamic equilibrium) regime. It was shown that, in the case of Xenon, NLTE effects can be neglected for  $T < 30 \text{ eV}$  on the ionic stage. Whereas we note a good agreement for the mean charge between the two models; there is a discrepancy of a factor of about two between the two opacities. Thus, in the Helios computations presented below, the opacity will be multiplied by two for Argon and by a factor of 20 for Xenon.<sup>40</sup>

The typical variations of the electron density temperature, the mean ion charge, and the electronic density are reproduced at 15 ns for Argon and Xenon at 600 mbar (Fig. 8). We are using the temporal profile of the PALS driving laser. The laser energy is set to  $50\,000 \text{ J/cm}^2$  to provide a reasonable shock velocity of  $\sim 70 \text{ km/s}$ . This value is below the nominal value for a laser at  $\sim 100 \text{ J}$ , focused over  $350 \mu\text{m}$ , which would lead to an overestimation of the shock velocity, taking the available data provided by the software. The simulations are performed with ten groups of frequencies. The variations of the precursor electron density, which are of interest to the present study, can be easily deduced from the mean charge using the relation  $N_e = Z \cdot N_i$ , where  $N_i$  is reported in Table III for Argon and Xenon at 600 mbar (Table IV). The maximum expected electron densities of the precursor are, respectively,  $1 \times 10^{20}$  and  $2 \times 10^{20} \text{ cm}^{-3}$  for Argon and Xenon, whereas the maximum electron temperatures of the precursor are, respectively, equal to 19 and 34 eV and the corresponding ionic stages are 7 and 13.

The temperature profile is smoother in Argon than in Xenon, and the temperature is lower due to a larger radiative mean free path. Due to radiation effect and ionization, the compression at the shock front is large (20 for Argon and 16 for Xenon) compared to the factor of four obtained for the adiabatic shock wave.<sup>16</sup>

The simulation favors a supercritical regime, which means that the electron temperature just before and just after the discontinuity (near 0.1 cm) is equal. The nominal values of the temperature, electron density, and mean charge are reported for Argon and Xenon at 600 mbar (Table IV).

In the case of Argon at 200 mbar, the shock is weaker in agreement with the experimental results. The front is at about the same

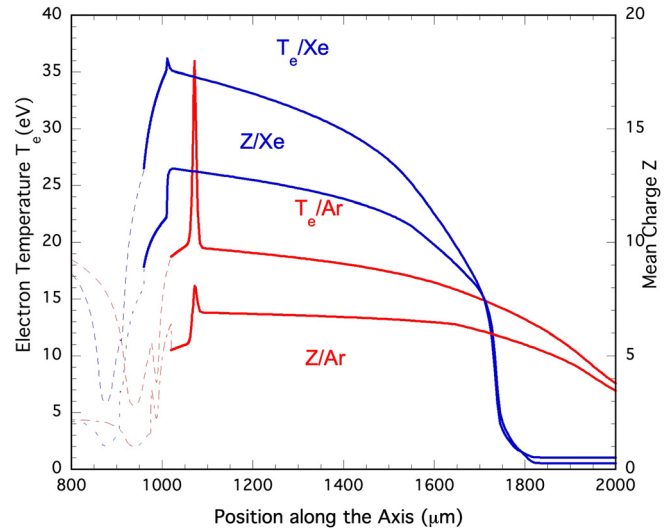


**FIG. 8.** Electron temperature and mean charge for Argon and Xenon obtained with HELIOS software at 15 ns for a ratio of the laser energy of the laser to the surface of its spot E/S equal to  $50\,000 \text{ J/cm}^2$ . Initial pressure 600 mbar. These quantities are plotted in solid lines for the gas, whereas they are plotted in dashed lines for the heated moving CH-Au foil. The front shock is located at 0.101 mm for Xenon and 0.107 for Argon, and the interface between the gas and the piston is, respectively, at 0.097 and 0.102 mm.

position (0.11 cm) as at 600 mbar. The extended precursor is heated at a temperature between 13 eV just before the front (instead of 20 eV at 600 mbar) and still up to 5 eV at 3.5 mm, close to the tube end, whereas the maximum mean charge is equal to six. The electron density peaks at  $3 \times 10^{19} \text{ cm}^{-3}$  just before the shock discontinuity and reaches  $9 \times 10^{20} \text{ cm}^{-3}$  in the post-shock.

These simulations illustrate the global structure of the radiative shock wave, with an extended precursor; those ionization, extension, and dynamics depend on the nature of the gas and of its pressure. However, the extension of the precursor is larger than in the experiment, which means that its internal radiative heating is too large, and let us expect that the electron density and temperature are in excess compared with the experimental case. This will be analyzed in the next section.

**B. 2D simulations**

In this context, we performed numerical simulations of the experiment with the 2D adaptative mesh refinement (AMR) radiative

**TABLE IV.** Typical values for the shock from HELIOS simulations for Argon and Xenon at 600 mbar, for a shock velocity of  $\sim 70 \text{ km/s}$ .

	Mean charge Z	Electron density $N_e \text{ (cm}^{-3}\text{)}$	Electron temperature $T_e \text{ (eV)}$	Mass density $\rho \text{ (g cm}^{-3}\text{)}$
Ar precursor	<7	<1E + 20	<20	0.001
Ar post-shock	<6	2E + 21	20	0.02
Xe precursor	<13	<2E + 20	<35	0.003
Xe post-shock	11	3E + 21	30	0.06

hydrodynamics code ARWEN.<sup>51</sup> This code has been used previously to successfully simulate the formation of a radiative shock wave<sup>30</sup> and other Laboratory Astrophysics systems.<sup>52</sup> The ARWEN code includes a high-order Godunov method for multimaterial hydrodynamics, a diffusion solver for electron heat conduction, a multigroup radiation transport solver and a model for laser energy deposition. The equations of state used in the simulations are based on the QEOS model fitted to experimental data,<sup>53</sup> and the opacities were generated with the BigBART code.<sup>54</sup> For these simulations, we collapsed the spectral opacities into eight groups.

The target was modeled as an aluminum tube of the inner radius of 300  $\mu\text{m}$  and length 950  $\mu\text{m}$  filled with Xenon gas at  $3.1 \times 10^{-3} \text{gcm}^{-3}$  or with Argon gas at  $1.0 \times 10^{-3} \text{gcm}^{-3}$  (both corresponding to a pressure of 0.6 bar). The laser energy is 100 J at 433 nm and FWHM of 350 ps with the Gaussian temporal profile. The spot diameter of the laser is 330  $\mu\text{m}$  with a hypergaussian profile. Simulation conditions are similar in terms of energy to the experimental shot 50 387 (Fig. 5) for Xenon except for the laser spot size, which is  $280 \pm 30 \mu\text{m}$ . These conditions are also close to shot 50 365 (Fig. 3, with a focal spot of  $330 \pm 30 \mu\text{m}$  with a little higher energy of 144 J). In Fig. 9, we show electron density and electron temperature profiles for the Xenon simulation from the average of the 2D results around the axis of the system. We can appreciate from the electron density and temperature profiles that the precursor is very stable after its formation at around 5 ns after the laser irradiation. This quasi-stationary limit was already mentioned in previous experiments.<sup>36</sup> The main reason is that the velocity of the pushing CH–Au piston does not change much during its free propagation in the tube. As a consequence, the radiative flux, which emerges from the front shock and heats the gas ahead, is relatively stable with time. Thus, after the rapid rise up of the radiative heating (here about 5 ns), the dynamics of the radiative precursor is relatively stable.<sup>55</sup>

The average density of the shocked Xe behind the shock is  $0.047 \text{g cm}^{-3}$ , which makes for this post-shock a compressibility ratio of 14.9.

In Fig. 10, we show the comparison of the electron temperature for the simulations with Argon and Xenon as filling gases, using as reference for the position along the system axis the position of the shock wave. The only difference in the simulation parameters between both cases is the density of the filling gas, selected to match an initial pressure of 0.6 bar for Argon and Xenon. We tracked the shock wave position with the average of the system properties in a volume around the axis. The averaged shock wave velocity for Argon is  $64.5 \text{ km s}^{-1}$  and for Xenon, it is  $55.7 \text{ km s}^{-1}$ . The peak electron temperature ranges from 18.3 to 22.1 eV in Argon and from 23.9 to 25.8 eV in Xenon, leading to ionization states around  $\text{Ar}^{+6}$  and  $\text{Xe}^{+9}$ , respectively. Thus, as expected, the heating and extension of the precursor are lower than in 1D simulations shown in Fig. 8 due to the consideration of the radiative lateral losses of the radiative shock. We appreciate from the isocontours of electron density that the precursor in Xenon is much larger than in Argon. The simulations present a larger curvature of the shock wave compared to the experimental as shown in data in Fig. 14. This might be attributed to the differences in the lateral section of the cell where the shocks develop, which is a circle of diameter equal to 600  $\mu\text{m}$  in the simulation, whereas it is a rectangle in the experiment, with dimensions equal to 4 mm along the path of the probing laser and 900  $\mu\text{m}$  in the dimension of the interferometric image. The shock wave then can expand more in this last dimension.

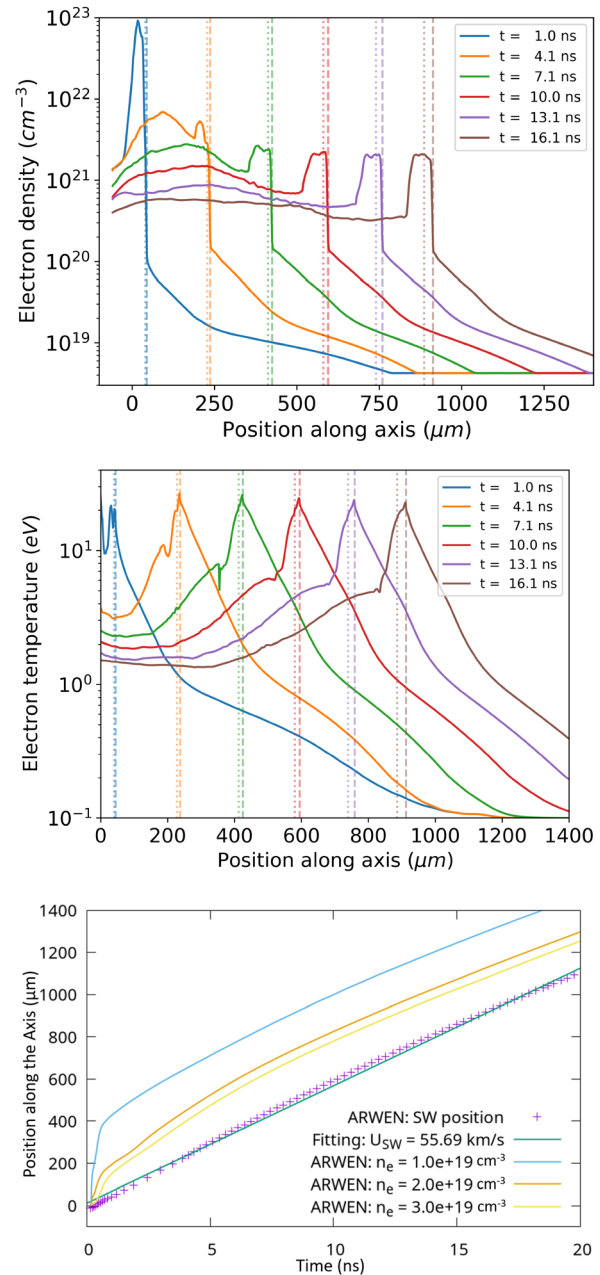


**FIG. 9.** Results of the 2D simulations in Xenon with ARWEN. We show the averaged profiles around the axis for a radius of 17.5  $\mu\text{m}$  for electron density, electron temperature, and the position of the shock wave (SW). For electron density and electron temperature, we show the shock wave position with dashed lines and the interface between the gold plate and the Xe with dotted lines. 2D simulation results from a cylindrical target of radius 300  $\mu\text{m}$  and length 950  $\mu\text{m}$  filled with Xe gas at 0.6 bar. The laser energy is 100 J at 433 nm and the spot diameter is 330  $\mu\text{m}$ . The QEOS model used in the simulations overestimates the ionization state for low temperatures (in this case,  $\text{Xe}^{+0.29}$  at the initial conditions), resulting in a minimum of electron density of  $4.2 \times 10^{18} \text{cm}^{-3}$  for the simulations. As expected, the peak electron temperature is achieved just behind the shock wave in the compressed Xe gas.

19 March 2024 15:38:11

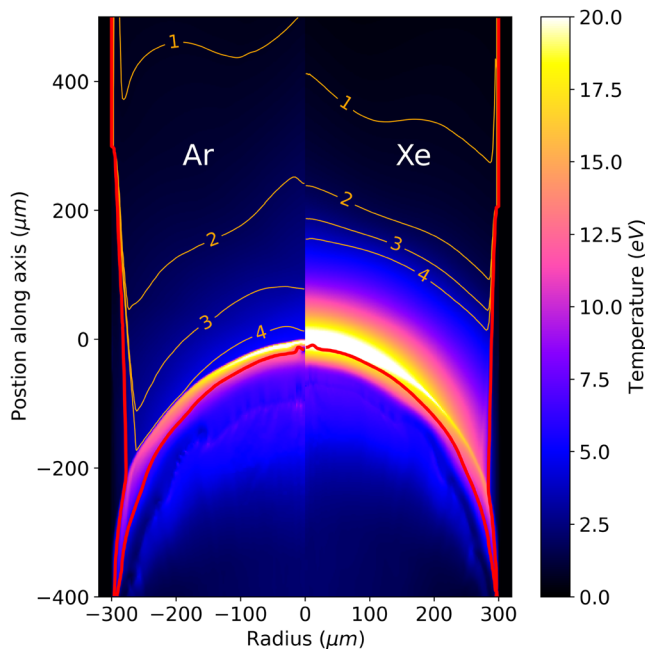


**FIG. 10.** Comparison of the simulations of radiative precursor in Argon (left) and in Xenon (right) at 8 ns. The orange lines are the isocontours of electron density of  $1 \times 10^{19}$ ,  $2 \times 10^{19}$ ,  $3 \times 10^{19}$ , and  $4 \times 10^{19} \text{ cm}^{-3}$ , and the red line is the material interface between the filling gas and the gold plate. The shock wave front is ahead of the material interface (above the red line). The position along the symmetry axis refers to the shock wave position at the axis for each case. Target and laser parameters are the same for both cases. Also, the pressure of the filling gas is 0.6 bar for Ar and Xe. The oscillations in the electron density isocontours of  $1 \times 10^{19}$  and  $2 \times 10^{19} \text{ cm}^{-3}$  are produced by the numerical method of the radiation transport solver and are not physical.

We compared the numerical results for the electron density with those of the different experimental shots. We found the best agreement with the shot 50 365 (Fig. 3) at 5 and 17 ns, as can be seen from Fig. 11. For this shot, the laser energy is higher than for the simulation (144 J against 100 J). However, this comparison is limited because the target section is, in the simulation, smaller than in the experiment ( $0.28$  against  $0.54 \text{ mm}^2$ ). In addition, the walls in the simulation are in aluminum, whereas those of the targets are mixed, with, in particular, a thin SiN membrane on the top, which is almost transparent to the XUV photons. Thus, for the same laser energy and focal spot, the experimental radiative wave expands more laterally than in the simulation and a larger laser energy is thus required to achieve the same precursor velocities. A complete analysis would then be numerically necessary.

This numerical modeling using 1D and 2D models confirms the presence of a radiative precursor, which is hotter in 1D than in 2D, where the effects of the radiation losses at the walls of the shock tube take an important role. The analysis confirms for the precursor an expected electron density larger than  $1 \times 10^{19} \text{ cm}^{-3}$ , in agreement with the experimental results. The radiative precursor is less extended and less ionized for Argon than for Xenon (Fig. 10), confirming the experimental results at 600 mbar. The expected maximum mean ionic charges predicted by this simulation are, respectively, equal to six and

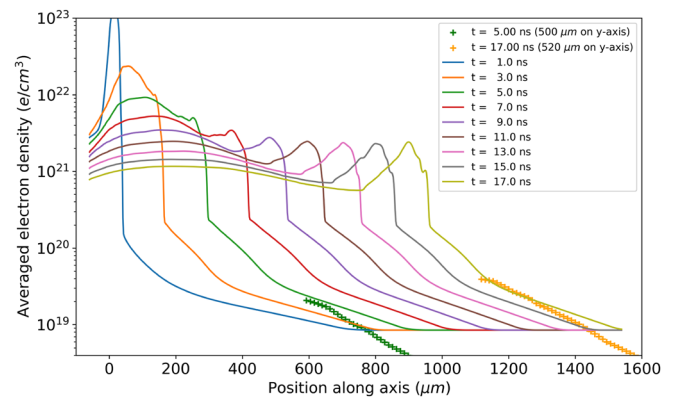


**FIG. 11.** Integrated electron density from the Xenon simulation compared with experimental data for shot 50 365. The comparison is limited because simulations have a lower bound for the electron density as mentioned in Fig. 9. The simulation matches the position of the precursor.

nine. These last results require now to be validated by our XUV spectroscopic diagnostics, which will be the object of Sec. V.

## V. XUV SPECTRA OF RADIATIVE SHOCKS IN ARGON AND XENON

### A. A qualitative overview

A qualitative analysis of the expected spectroscopic records has been performed using the PrismSPECT<sup>56</sup> software. The goal is here to inspect, with the temperature and electron density range given by the previous experimental and numerical study, the relative contributions of the emitted radiative flux in the post-shock and in the precursor, and to identify, in the case of Argon (which has a simpler spectrum than Xenon) the presence of possible strong lines for the XUV diagnostics.

The emissivity of a thin layer ( $50 \mu\text{m}$  thick) of plasma at uniform density and temperature is reported in Fig. 12 at two temperatures (10 and 30 eV) for Argon at  $0.001$  and  $0.015 \text{ g cm}^{-3}$ , between 5 and 30 nm, which is the wavelength range covered by our XUV diagnostic.

One may first note that the spectrum is richer in lines at the highest temperature and density. At 30 eV, the intensity is about 100 times higher for the highest mass density than for the lowest one.

At the lowest temperature of 10 eV, the spectrum consists of a continuum for the highest density and will thus not be observed in the experiment.

However, the denser post-shock has a more minor extension than the low-density precursor; thus, the contribution of the latter to the space and time-integrated data cannot be neglected at first glance.

Common intense lines are observed at 30 eV, high and low densities, and at 10 eV, low density, at 12, 14, 16, 18, 23, and 26 nm. These lines are expected to appear in the recorded spectrum, which is the object of Sec. V B.

In addition, as expected by the presence of a radiative precursor, the emerging spectrum is affected by radiation transfer effects.<sup>57</sup> Thus, to collect the maximum of photons on the detector, it is then suitable to reduce the thickness of the cold gas layers between the shock and the detector.<sup>36</sup>

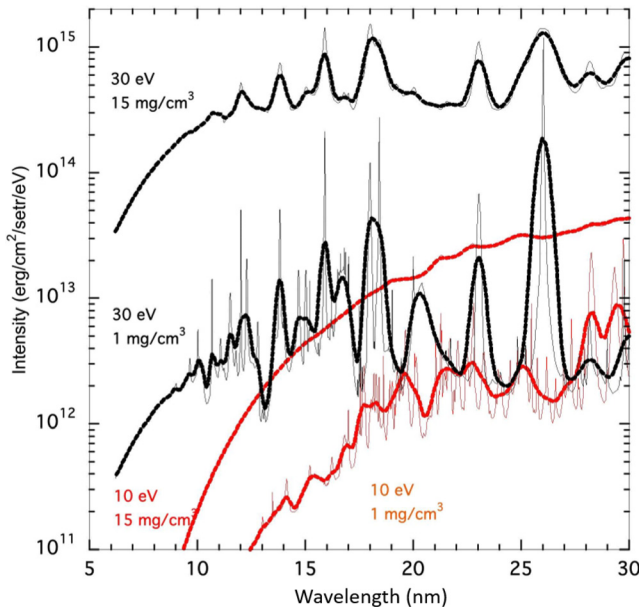


**FIG. 12.** Emissivity of an Argon plasma with a thickness of  $50\ \mu\text{m}$ , obtained with PrismSPECT at LTE for two temperatures (10 eV in red and 30 eV in black), and two mass densities ( $0.015$  and  $0.001\ \text{g cm}^{-3}$ ). This emissivity is plotted without any additive broadening to the spectral resolution (thin lines). To facilitate the analysis, the spectrum is also plotted with a spectral resolution  $\lambda/\Delta\lambda$  equal to 40 (thick lines).

**B. XUV spectroscopic Experimental results**

As indicated previously, the wavelength calibration is performed using the Al edges in the first and second orders using different records, the dispersion rule for an aberration-corrected concave grating,<sup>58,59</sup> and some adjustments.<sup>60</sup>

Contrary to our previous experiment<sup>40</sup> using together a CCD camera and an Aluminum filtering covering all the radiation of the target, the records are here wider in terms of wavelengths. It extends from 10 to 35 nm.

In the present case, the absence of an Aluminum filter that blocks the light below 17 nm introduces the complication of the contribution of the different diffraction orders in the net spectra. This is why we shall limit our study to wavelength comprised between 10 and 22 nm, where the signal is at maximum.

We present below the results obtained for Argon (shot 50 389; laser energy 134 J) and Xenon (shot 50 382; laser energy 183 J) at 0.6 and 0.5 bar, respectively. In these shots, the laser focalization is similar to the one used previously for shot 50 387 (tight focus, Sec. III B). High intensity, relatively high pressures, and a focalization slightly centered upwards on the tube (to reduce the absorption by the gas) are necessary to obtain at least a moderate-quality signal.

The recorded spectra, presented in Fig. 13, are composed of a multitude of relatively faint lines superposed to a strong continuum, which is expected from the contribution of the denser post-shock and also from the heated CH–Au material behind the shock. However, our purpose is not to identify all these lines but some of them to deduce information about the ionization stages present in the plasma.

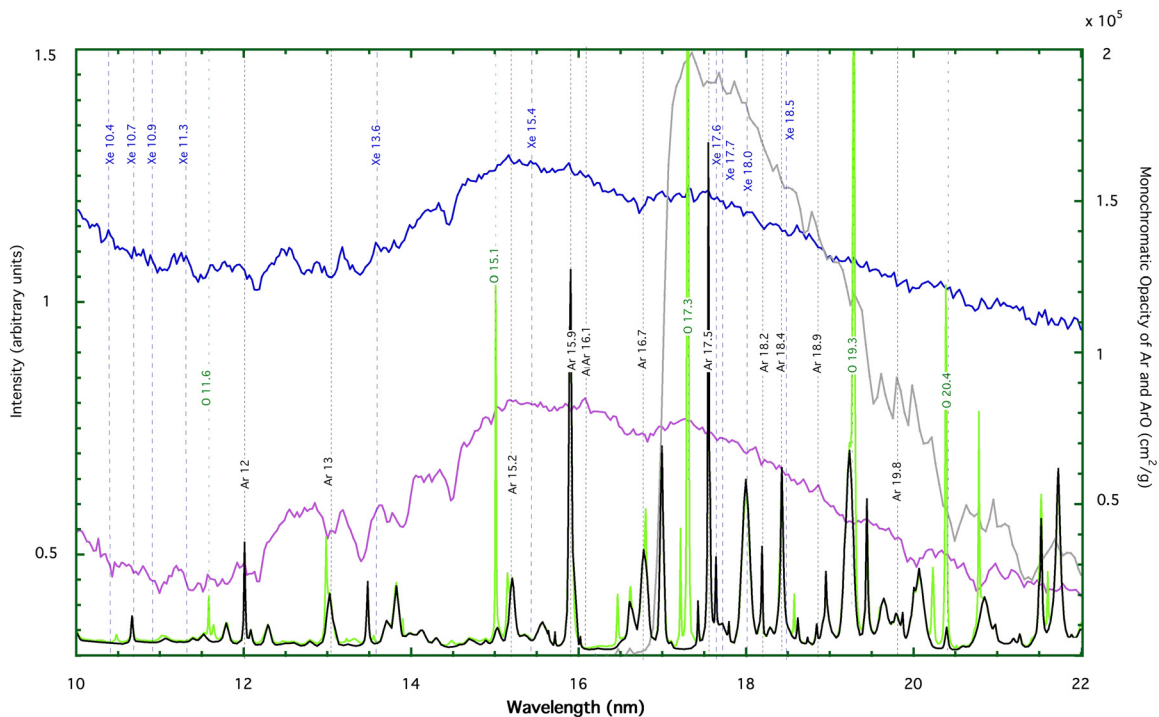


**FIG. 13.** Time and space integrated XUV spectra of Argon (shot 50 389; in pink) and Xe (shot 50 382; in blue) between 10 and 22 nm. The interval between two pixels corresponds to  $\sim 0.04\ \text{nm}$ , and the spectral resolution  $\sim 0.05\ \text{nm}$  near 15 nm. A previous record of Xenon (shot 48 143; in gray) is presented for comparison.<sup>40</sup> The monochromatic opacity obtained with PRISMPECT software, at LTE, for Ar (in black) and Ar(90%)–O(10%) (in green), both at a mass density of  $10^{-3}\ \text{g/cm}^3$  and a temperature of 15 eV, is reported for information.

19 March 2024 15:38:11

Our procedure takes advantage of the presence of Oxygen lines in the Argon and Xenon spectra. Thus, to help with the determination, we first compute as a reference the monochromatic opacity of Argon and a mixture of Argon with Oxygen in conditions reasonably close to the experiment ( $1 \text{ mg cm}^{-3}$  and  $15 \text{ eV}$ ). These monochromatic opacities are computed with PrismSPECT<sup>56</sup> software, which for Argon, gives line positions, in agreement with the NIST database.<sup>61</sup> The differences between the two monochromatic opacities are unambiguously accredited to Oxygen lines. Among them, we retain only those that are also present in the Ar and Xe experimental spectra. The corresponding lines are attributed to  $\text{O}^{4+}$  and  $\text{O}^{5+}$ , which is coherent with a plasma at  $15\text{--}30 \text{ eV}$ .

After this stage, we focus our attention on the lines present in the Ar spectrum and not in the Xe spectrum. For Argon, with the help of the previous monochromatic opacities and also of the NIST database, the residual lines are mostly ascribed to  $\text{Ar}^{7+}$ . Few lines are attributed to  $\text{Ar}^{6+}$ . This is consistent with the ionization stage obtained in the simulations and a plasma comprised of between  $15$  and  $30 \text{ eV}$ . Assuming that the density of the radiatively heated precursor remains equal to its unperturbed value, these values are also consistent with an electron density reaching local values in the range of  $10^{20} \text{ cm}^{-3}$ .

The situation of Xenon is more complex due to its rich spectrum. However, the lines, which we have identified using the NIST reference data, are assigned to  $\text{Xe}^{7+}$ ,  $\text{Xe}^{8+}$ ,  $\text{Xe}^{9+}$ , and  $\text{Xe}^{10+}$ , with a possible line at  $11.3 \text{ nm}$ , which can be attributed either to  $\text{Xe}^{10+}$  or  $\text{Xe}^{6+}$  (1 line). This is consistent with an ionization stage between seven and ten, corresponding to an electron density between  $1$  and  $1.5 \times 10^{20} \text{ cm}^{-3}$ , in agreement with the interferometric measurement [Fig. 14(b)].

The summary of the identified transitions is reported in Table V.

## VI. SUMMARY AND PERSPECTIVES

In conclusion, we have performed a detailed comparative study of the topology, dynamics, and electron density of radiative precursors developing in two noble gases, Argon and Xenon, at two initial pressures ( $0.2$  and  $0.6 \text{ bar}$ ). This study was obtained due to high-quality targets and a time-resolved instantaneous imaging setup using a based femtosecond laser, which was used for the first time in such circumstances. This setup presented high-quality images without blurring and with a high fringe contrast. It showed its interest in future radiative shock experiments at higher velocities. It was also shown that even small deflections of the probing laser beam, compared to the reference beam, induced by high-density electron bent zones may lead to the disappearance of the fringes. This unexpected effect, together with a precise measurement of the initial time overlap, and of the distances of interest, could be used as an auxiliary indicator of the bent shape of the plasma. In addition, we proved the feasibility of the use of image plates as a detector in the XUV range. Even if a new plate was used at each shot, these cheap detectors, compared to CCD, present the advantage of being insensitive to EMP and to residual IR laser light visible light. Thus, they do not need to be protected by additive filters. As a consequence, we recorded for the first time the spectra for the two gases, from  $10$  to  $30 \text{ nm}$ . Many lines were identified. The interferometric records were interpreted due to the combination of 1D simulations, as a first insight and 2D simulations for more detailed analysis.

The interferometric images show a bending in the precursor from Argon and Xenon, whatever the initial pressure. For the same initial laser conditions and gas pressure, the precursor extension is longer for Argon than for Xenon. This is due to the larger light absorption

mean free path for Argon than for Xenon over the temperature domain.

Across all shots, a consistent trend is observed where the ionization wave monotonically decreases with time up to  $15 \text{ ns}$  and tends to stabilize after, except for Argon at  $0.2 \text{ bar}$ . In this specific case, the precursor velocity remains nearly constant (or slightly increases) during the initial  $15 \text{ ns}$  before slightly decreasing with time. We believe that this slow heating process, as compared with Argon at a higher pressure of  $0.6 \text{ bar}$ , comes from the reduced opacity, due to a smaller number of absorbing particles. In addition, at the same pressure, our experiment and the 1D and 2D simulations show that Argon is less heated as compared with Xenon, which has a larger opacity.

An interesting result about the influence of the diameter of laser spot size is presented in this paper, when the energy is concentrated in a smaller focus (tight focus case); we note a higher velocity at an early time, followed by a lower one at longer times. This is due to a stronger bending of the shock, which loses more energy laterally. However, the extreme case of a blast wave, where the laser energy is concentrated in a small focal spot, presents the advantage of a simpler symmetry (1D spherical) and a negligible contribution of the lateral windows of the target, supposed to be at a larger distance than in the present case.

The radiative heating and the velocity deduced from 1D simulations are higher in 1D simulations than in the experiment. The comparison with 2D simulations confirms the already shown effect of the lateral radiative losses at the walls of the target, which depends on the walls albedo as mentioned in González and Audit.<sup>29</sup>

The 2D simulations show good stability of the radiative shock wave after its formation for both Argon and Xenon cases, keeping the velocity of the shock wave almost constant over the time span of the analysis. Xenon exhibits a more intense coupling between hydrodynamics and radiation transport, thus producing a radiative shock wave with higher temperatures and a much larger precursor than in Argon although the Argon simulation has a higher shock wave velocity. At later times, the shock wave front becomes unstable for both cases and we need further analysis to study its effect on the precursor.

This work shows the advantage of using Argon as a template for experimental radiative shocks in place of Xenon. Indeed, due to its simpler ionic structure, the opacity and equation of state are, in practice, more precise than for Xenon. It goes also for the spectroscopic signatures. This eliminates the important difficulty of the opacity accuracy in the radiative hydrodynamics simulations. As a consequence, they are more adapted if the goal is to test the quality of radiative hydrodynamic simulations, which remains today a difficult challenge. The use of Argon and Ar-O mixture would even help more for the line identification and wavelength calibration.

Our preliminary numerical analysis shows that the expected spectrum is rich in lines from  $10$  up to at least  $30 \text{ nm}$ , which is confirmed by the experiment. Despite the absence of space and time resolution, the analysis of the spectra is a good indicator of the ionic stages obtained in the shock. The spectra are rich in lines. However, the presence of Oxygen lines and the comparison of the Xenon and Argon spectra allow line identification. Oxygen is present from  $\text{O}^{4+}$  to  $\text{O}^{5+}$  (which is coherent with a plasma at  $15\text{--}30 \text{ eV}$ ), and Argon is present as  $\text{Ar}^{6+}$  to  $\text{Ar}^{7+}$ , which is also coherent with the same temperature range.

This work shows that challenging spectroscopic investigations become feasible with adequate instrumentation. We hope that these preliminary results will facilitate future studies at the higher spectral

resolution, which would facilitate the identification of the lines over the strong continuum. The next step should be to implement spatial and time resolution, which will require a new generation XUV spectroscopic diagnostic.

## ACKNOWLEDGMENTS

We thank the PALS (Prague Asterix Laser System) installation, the Czech Ministry of Education, Youth and Sports (CMEYS) for the financial support of the project nr. LM2023068. C. Stehlé acknowledges the support from the Labex Plas@Par (ANR-11-IDEX-0004-02) and of the Programme National de Physique Stellaire of CNRS/INSU, Observatoire de Paris. R. Rodriguez acknowledges the support of the Spanish Government through the project PID2019-110678GB-I00. M. Cotelo and P. Velarde acknowledge the support of the Spanish Government through the project PID2021-124129OB-I00 funded by MCIN/AEI/10.13039/501100011033/ERDF, EU. We thank J. Larour (retired from LPP, CNRS, Ecole Polytechnique, Sorbonne-University, France) for his support during the experiment. We thank Tomasz Chodukowski (Institute of Plasma Physics and Laser Microfusion, Warsaw) for taking part in a few discussions related to interferometric data analysis.

## AUTHOR DECLARATIONS

### Conflict of Interest

The authors have no conflicts to disclose.

### Author Contributions

**Raj Laxmi Singh:** Conceptualization (equal); Data curation (equal); Formal analysis (equal); Methodology (equal); Validation (equal); Visualization (equal); Writing—original draft (equal); Writing—review & editing (equal). **Francisco Suzuki-Vidal:** Data curation (supporting); Writing—review & editing (supporting). **Tadeusz Pisarczyk:** Methodology (equal); Supervision (supporting). **Chantal Stehle:** Conceptualization (equal); Data curation (equal); Formal analysis (equal); Funding acquisition (equal); Investigation (equal); Methodology (equal); Project administration (equal); Resources (equal); Software (equal); Supervision (equal); Validation (equal); Visualization (equal); Writing—original draft (equal); Writing—review & editing (equal). **Michaela Kozlova:** Conceptualization (supporting); Methodology (supporting); Writing—review & editing (supporting). **Manuel Cotelo:** Data curation (supporting); Formal analysis (supporting); Methodology (supporting); Software (equal); Writing—review & editing (equal). **Jan Dostal:** Methodology (supporting); Writing—review & editing (supporting). **Roman Dudzak:** Methodology (supporting); Writing—review & editing (supporting). **Rafael Rodríguez:** Supervision (equal); Writing—review & editing (equal). **Pedro Velarde:** Formal analysis (supporting); Software (equal); Supervision (supporting); Validation (supporting). **Patrice Barroso:** Methodology (supporting); Writing—review & editing (supporting).

## DATA AVAILABILITY

The data that support the findings of this study are available from the corresponding author upon reasonable request.

## APPENDIX: ADDITIONAL INTERFEROMETRY DATA

We present two interferometric images for Argon at 200 mbar under different laser conditions for the energy (respectively, 111 and 134 J) and focalization (respectively, 350 and 280  $\mu\text{m}$  diameter) in Fig. 14. They illustrate the influence of the laser intensity on the development of the precursor (Sec. II A).

In Table V, we present the ionization stage, the electron configuration, and the transitions for the identified lines from experimental XUV data in Fig. 13.

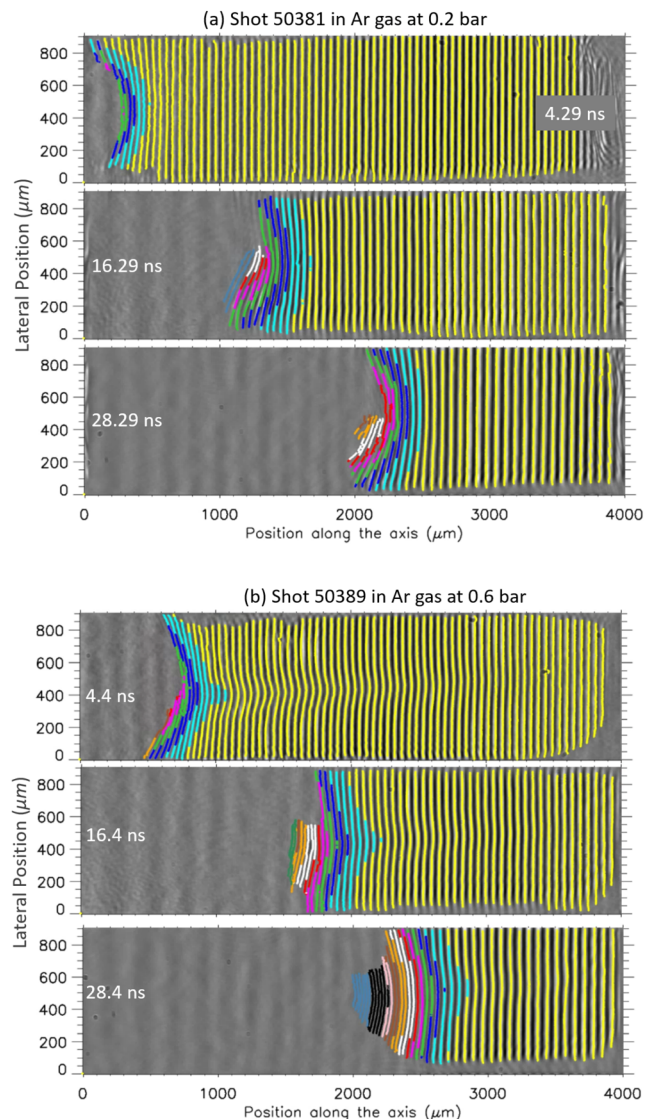


**FIG. 14.** (a) Shot 50381 with a 111 J laser energy for Ar gas at 0.2 bar, and images are recorded at 4.68, 16.68, 28.68 ns. (b) Shot 50389 with a 134 J laser energy and spot size for this shot is  $\sim 280 \mu\text{m}$  for Ar gas at 0.6 bar, and images are recorded at 4.4, 16.4, and 28.4 ns. The residual narrow spike in the center of the image comes from a preionization of the gas due to the presence of an identified tiny defect in the gold coating of the piston foil.

TABLE V. Identification of the relevant lines<sup>62</sup> of Fig. 13.

Wavelength (nm)	Ion	Lower state	Upper state
10.4	Xe IX	4d <sup>10</sup> 1S	4d <sup>9</sup> 6p <sup>3</sup> P
10.7	Xe VII	4d <sup>10</sup> 5s <sup>2</sup> 1S	4d <sup>9</sup> 5s <sup>2</sup> 5f <sup>1</sup> P
10.9	Xe XI	4p <sup>6</sup> 4d <sup>8</sup> 1P, <sup>3</sup> G, <sup>1</sup> D	4p <sup>5</sup> 4d <sup>9</sup>
11.3	Xe X	4d <sup>9</sup> 2D	4d <sup>8</sup> 4f
11.3	Xe XI	4p <sup>6</sup> 4d <sup>8</sup> 2D, <sup>3</sup> P, <sup>1</sup> G	4p <sup>6</sup> 4d <sup>7</sup> 4f
11.3	Xe VII	4d <sup>10</sup> 5s <sup>2</sup> 1S	4d <sup>9</sup> 5s <sup>2</sup> 5f <sup>3</sup> P
11.6	O VI	1s <sup>2</sup> 2s <sup>2</sup> 2S	1s <sup>2</sup> 4p <sup>2</sup> P
11.6	O VI	1s <sup>2</sup> 2p <sup>2</sup> 2P	1s <sup>2</sup> 5d <sup>2</sup> D
12	Ar VIII	2p <sup>6</sup> 3s <sup>2</sup> 2S	2p <sup>6</sup> 5p <sup>2</sup> P
15.1	O V	1s <sup>2</sup> 2s2p <sup>3</sup> P	1s <sup>2</sup> 2s4d <sup>3</sup> D
15.2	Ar VII	3s3p <sup>3</sup> P	3s5d <sup>3</sup> D
17	Ar VII	3s3d <sup>3</sup> D	3s8f <sup>3</sup> F
17	Ar VII	3s3p <sup>3</sup> P	3p4p <sup>3</sup> S
17.3	O VI	1s <sup>2</sup> 2p <sup>2</sup> 2P	1s <sup>2</sup> 3d <sup>2</sup> D
17.5	Ar VII	2p <sup>6</sup> 3s <sup>2</sup> 1S	3s4p <sup>1</sup> P
17.6	Xe VIII	4d <sup>10</sup> 5s <sup>2</sup> 2S	4d <sup>9</sup> 5s5p
17.7	Xe VIII	4d <sup>10</sup> 5s <sup>2</sup> 2S	4d <sup>9</sup> 5s5p
18	Xe VIII	4d <sup>10</sup> 5s <sup>2</sup> 2S	4d <sup>10</sup> 5s5p
18.2	Ar VII	3s3p <sup>1</sup> P	3p4p <sup>1</sup> D
18.4	Ar VIII	2p <sup>6</sup> 3d <sup>2</sup> D	2p <sup>6</sup> 5f <sup>2</sup> F
19.3	O V	1s <sup>2</sup> 2p <sup>2</sup> 1D	1s <sup>2</sup> 2s4f <sup>1</sup> F
19.3	O V	1s <sup>2</sup> 2s2p <sup>3</sup> P	1s <sup>2</sup> 2s3d <sup>3</sup> D
19.3	Ar VII	3s3p <sup>3</sup> P	3s4d <sup>3</sup> D
20.4	O V	1s <sup>2</sup> 2p <sup>2</sup> 3P	1s <sup>2</sup> 2p3d <sup>3</sup> D

## REFERENCES

- 1K. Goodrich, S. Schwartz, L. Wilson III, I. Cohen, D. Turner, A. Caspi, K. Smith, R. Rose, P. Whittlesey, F. Plaschke *et al.*, "The persistent mystery of collisionless shocks," [arXiv:2306.05491](https://arxiv.org/abs/2306.05491) (2023).
- 2A. Spitkovsky, "Particle acceleration in relativistic collisionless shocks: Fermi process at last?," *Astrophysical J.* **682**, L5 (2008).
- 3Z. Gong, X. Shen, K. Z. Hatsagortsyan, and C. H. Keitel, "Electron slingshot acceleration in relativistic preturbulent shocks explored via emitted photon polarization," *Phys. Rev. Lett.* **131**, 225101 (2023).
- 4R. Blandford and D. Eichler, "Particle acceleration at astrophysical shocks: A theory of cosmic ray origin," *Phys. Rep.* **154**, 1–75 (1987).
- 5C. Li, V. Tikhonchuk, Q. Moreno, H. Sio, E. d'Humieres, X. Ribeyre, P. Korneev, S. Atzeni, R. Betti, A. Birkel *et al.*, "Collisionless shocks driven by supersonic plasma flows with self-generated magnetic fields," *Phys. Rev. Lett.* **123**, 055002 (2019).
- 6J. Ross, D. Higginson, D. Ryutov, F. Fiuza, R. Hatarik, C. Huntington, D. Kalantar, A. Link, B. Pollock, B. Remington *et al.*, "Transition from collisional to collisionless regimes in interpenetrating plasma flows on the national ignition facility," *Phys. Rev. Lett.* **118**, 185003 (2017).
- 7D. B. Schaeffer, W. Fox, R. Follett, G. Fiksel, C. Li, J. Matteucci, A. Bhattacharjee, and K. Germaschewski, "Direct observations of particle dynamics in magnetized collisionless shock precursors in laser-produced plasmas," *Phys. Rev. Lett.* **122**, 245001 (2019).
- 8R. P. Drake, *Introduction to High-Energy-Density Physics* (Springer, 2018), pp. 1–20.
- 9Y. B. Zel'Dovich and Y. P. Raizer, *Physics of Shock Waves and High-Temperature Hydrodynamic Phenomena* (Courier Corporation, 2002).
- 10J. Grun, J. Stamper, C. Manka, J. Resnick, R. Burris, J. Crawford, and B. Ripin, "Instability of Taylor–Sedov blast waves propagating through a uniform gas," *Phys. Rev. Lett.* **66**, 2738 (1991).
- 11S. Bouquet, C. Stehlé, M. Koenig, J.-P. Chièze, A. Benuzzi-Mounaix, D. Batani, S. Leygnac, X. Fleury, H. Merdji, C. Michaut, F. Thais, N. Grandjouan, T. Hall, E. Henry, V. Malka, and J.-P. J. Lafon, "Observation of laser driven supercritical radiative shock precursors," *Phys. Rev. Lett.* **92**, 225001 (2004).
- 12G. Rigon, B. Albertazzi, P. Mabey, T. Michel, P. Barroso, A. Faenov, R. Kumar, C. Michaut, T. Pikuz, Y. Sakawa *et al.*, "Hydrodynamic instabilities in a highly radiative environment," *Phys. Plasmas* **29**, 072106 (2022).
- 13S. H. Langer, G. Channugam, and G. Shaviv, "Thermal instability in accretion flows onto degenerate stars," *Astrophysical J.* **245**, L23–L26 (1981).
- 14J. M. Laming and J. Grun, "Improved models for the dynamical overstability of radiative blast waves," *Phys. Plasmas* **10**, 1614–1618 (2003).
- 15R. Rodriguez, G. Espinosa, J. M. Gil, C. Stehlé, F. Suzuki-Vidal, J. G. Rubiano, P. Martel, and E. Mínguez, "Microscopic properties of xenon plasmas for density and temperature regimes of laboratory astrophysics experiments on radiative shocks," *Phys. Rev. E* **91**, 053106 (2015).
- 16C. Michaut, C. Stehlé, S. Leygnac, T. Lanz, and L. Boireau, "Jump conditions in hypersonic shocks," *Eur. Phys. J. D* **28**, 381–392 (2004).
- 17A. C. Raga, G. Mellema, S. J. Arthur, L. Binette, P. Ferruit, and W. Steffen, "3D transfer of the diffuse ionizing radiation in ism flows and the preionization of a Herbig–Haro working surface," *Rev. Mex. Astron. Astrofis.* **35**, 123–133 (1999).
- 18R. Bonito, S. Orlando, C. Argiroffi, M. Miceli, G. Peres, T. Matsakos, C. Stehle, and L. Ibgui, "Magnetohydrodynamic modeling of the accretion shocks in classical T Tauri stars: The role of local absorption in the x-ray emission," *Astrophys. J. Lett.* **795**, L34 (2014).
- 19L. de Sá, J.-P. Chièze, C. Stehlé, I. Hubeny, T. Lanz, and V. Cayatte, "New insight on accretion shocks onto young stellar objects: Chromospheric feedback and radiation transfer," *Astron. Astrophys.* **630**, A84 1–A84 17 (2019).
- 20S. Colombo, L. Ibgui, S. Orlando, R. Rodriguez, G. Espinosa, M. González, C. Stehlé, L. de Sa, C. Argiroffi, R. B., and G. Peres, "Effects of radiation in accretion regions of classical T Tauri stars: Pre-heating of accretion column in non-LTE regime," *Astron. Astrophys.* **629**, L9 (2019).
- 21U. M. Noebauer, S. A. Sim, M. Kromer, F. K. Röpkke, and W. Hillebrandt, "Monte Carlo radiation hydrodynamics: Methods, tests and application to Type Ia supernova ejecta," *Mon. Not. R. Astron. Soc.* **425**, 1430–1444 (2012).
- 22W. V. Jacobson-Galán, L. Dessart, D. O. Jones, R. Margutti, D. L. Coppejans, G. Dimitriadis, R. J. Foley, C. D. Kilpatrick, D. J. Matthews, and S. Rest, "Final moments. I. Precursor emission, envelope inflation, and enhanced mass loss preceding the luminous type II supernova 2020tlf," *Astrophys. J.* **924**, 15 (2022).
- 23D. Mihalas and B. W. Mihalas, *Foundations of Radiation Hydrodynamics* (Courier Corporation, 2013).
- 24R. P. Drake, "Theory of radiative shocks in optically thick media," *Phys. Plasmas* **14**, 043301 (2007).
- 25C. Michaut, E. Falize, C. Cavet, S. Bouquet, M. Koenig, T. Vinci, A. Reighard, and R. P. Drake, "Classification of and recent research involving radiative shocks," *Astrophys. Space Sci.* **322**, 77–84 (2009).
- 26R. M. Lowrie and R. B. Rauenzahn, "Radiative shock solutions in the equilibrium diffusion limit," *Shock Waves* **16**, 445–453 (2007).
- 27M. W. Sincell, M. Gehmeyr, and D. Mihalas, "The quasi-stationary structure of radiating shock waves. I. The one-temperature fluid," *Shock Waves* **9**, 391–402 (1999).
- 28B. Fryxell, E. Rutter, and E. S. Myra, "Simulations of laser experiments of radiative and non-radiative shocks," *High Energy Density Phys.* **8**, 141–149 (2012).
- 29M. González, C. Audit, and E. Stehlé, "2D numerical study of the radiation influence on shock structure relevant to laboratory astrophysics," *Astron. Astrophys.* **497**, 27–34 (2009).
- 30M. Cotel, P. Velarde, A. de la Varga, D. Portillo, C. Stehlé, U. Chaulagain, M. Kozlova, J. Larour, and F. Suzuki-Vidal, "Simulation of radiative shock waves in Xe of last PALS experiments," *High Energy Density Phys.* **17**, 68–73 (2015). 10th International Conference on High Energy Density Laboratory Astrophysics.
- 31S. J. Meng, F. Ye, Z. P. Xu, X. S. Yan, S. Q. Jiang, J. Lu, Z. C. Huang, Q. Yi, F. X. Chen, and R. H. Yang, "Visualizing magnetically driven converging radiative shock generated in z-pinch foil liner implosion," *Phys. Plasmas* **28**, 122713 (2021).
- 32K. Kondo, M. Nakajima, T. Kawamura, and K. Horioka, "Relaxation layer in electro-magnetically driven strong shocks," *J. Phys.* **112**, 042028 (2008).

- <sup>33</sup>J. Larour, R. Singh, C. Stehlé, A. Ciardi, U. Chaulagain, and F. Suzuki-Vidal, "Optimization of an electromagnetic generator for strong shocks in low pressure gas," *High Energy Density Phys.* **17**, 129–134 (2015).
- <sup>34</sup>J. C. Bozier, G. Thiell, J. P. Le Breton, S. Azra, M. Decroisette, and D. Schirmann, "Experimental observation of a radiative wave generated in xenon by a laser-driven supercritical shock," *Phys. Rev. Lett.* **57**, 1304 (1986).
- <sup>35</sup>A. B. Reighard, R. P. Drake, K. K. Dannenberg, D. J. Kremer, M. Grosskopf, E. C. Harding, D. R. Leibbrandt, S. G. Glendinning, T. S. Perry, B. A. Remington, J. Greenough, J. Knauer, T. Boehly, S. Bouquet, L. Boireau, M. Koenig, and T. Vinci, "Observation of collapsing radiative shocks in laboratory experiments," *Phys. Plasmas* **13**, 082901 (2006).
- <sup>36</sup>C. Stehlé, M. González, M. Kozlova, B. Rus, T. Mocek, O. Acef, J. Colombier, T. Lanz, N. Champion, K. Jakubczak, J. Polan, P. Barroso, D. Bauduin, E. Audit, J. Dostal, and M. Stupka, "Experimental study of radiative shocks at PALS facility," *Laser Part. Beams* **28**, 253–261 (2010).
- <sup>37</sup>C. Stehlé, M. Kozlová, J. Larour, J. Nejdil, N. Champion, P. Barroso, F. Suzuki-Vidal, O. Acef, P.-A. Delattre, and J. Dostál, "New probing techniques of radiative shocks," *Opt. Commun.* **285**, 64–69 (2012).
- <sup>38</sup>U. Chaulagain, C. Stehlé, J. Larour, M. Kozlová, F. Suzuki-Vidal, P. Barroso, M. Cotel, P. Velarde, R. Rodriguez, and J. M. Gil, "Structure of a laser-driven radiative shock," *High Energy Density Phys.* **17**, 106–113 (2015).
- <sup>39</sup>F. Suzuki-Vidal, T. Clayson, C. Stehlé, G. F. Swadling, J. M. Foster, J. Skidmore, P. Graham, G. C. Burdiak, S. V. Lebedev, U. Chaulagain, R. L. Singh, E. T. Gumbrell, S. Patankar, C. Spindloe, J. Larour, M. Kozlova, R. Rodriguez, J. M. Gil, G. Espinosa, P. Velarde, and C. Danson, "Counterpropagating radiative shock experiments on the ORION laser," *Phys. Rev. Lett.* **119**, 055001 (2017).
- <sup>40</sup>R. L. Singh, C. Stehle, F. Suzuki-Vidal, M. Kozlová, J. Larour, U. Chaulagain, T. Clayson, R. Rodriguez, J. Gil, J. Nejdil *et al.*, "Experimental study of the interaction of two laser-driven radiative shocks at the PALS laser," *High Energy Density Phys.* **23**, 20–30 (2017).
- <sup>41</sup>F. Suzuki-Vidal, T. Clayson, C. Stehlé, U. Chaulagain, J. W. D. Halliday, M. Sun, L. Ren, N. Kang, H. Liu, and B. Zhu, "First radiative shock experiments on the SG-II laser," *High Power Laser Sci. Eng.* **9**, e27 (2021).
- <sup>42</sup>T. Clayson, F. Suzuki-Vidal, S. V. Lebedev, G. F. Swadling, C. Stehle, G. C. Burdiak, J. M. Foster, J. Skidmore, P. Graham, E. Gumbrell, S. Patankar, C. Spindloe, U. Chaulagain, M. Kozlova, J. Larour, R. L. Singh, R. Rodriguez, G. J. M. Gil, P. Velarde, and C. Danson, "Counter-propagating radiative shock experiments on the orion laser and the formation of radiative precursors," *High Energy Density Phys.* **23**, 60–72 (2017).
- <sup>43</sup>J. C. Bozier, J. P. Le Breton, T. Jalinaud, and J. Valadon, "A new supercritical shock wave regime," *Astrophys. J., Suppl. Ser.* **127**, 253 (2000).
- <sup>44</sup>M. Koenig, T. Vinci, A. Benuzzi-Mounaix, N. Ozaki, A. Ravasio, M. Rabec le Glohaec, L. Boireau, C. Michaut, S. Bouquet, and S. Atzeni, "Radiative shocks: An opportunity to study laboratory astrophysics," *Phys. Plasmas* **13**, 056504 (2006).
- <sup>45</sup>K. Jungwirth, A. Cejnarova, L. Juha, B. Kralikova, J. Krasa, E. Krousky, P. Krupickova, L. Laska, K. Masek, T. Mocek, M. Pfeifer, A. Prág, O. Renner, K. Rohlena, B. Rus, J. Skala, P. Straka, and J. Ullschmied, "The prague asterix laser system," *Phys. Plasmas* **8**, 2495–2501 (2001).
- <sup>46</sup>J. Dostal, R. Dudzak, T. Pisarczyk, M. Pfeifer, J. Huynh, T. Chodukowski, Z. Kalinowska, E. Krousky, J. Skala, and J. Hrebicek, "Synchronizing single-shot high-energy iodine photodissociation laser PALS and high-repetition-rate femtosecond Ti: Sapphire laser system," *Rev. Sci. Instrum.* **88**, 045109 (2017).
- <sup>47</sup>A. Kasperczuk and T. Pisarczyk, "Application of automated interferometric system for investigation of the behaviour of a laser-produced plasma in strong external magnetic fields," *Opt. Appl.* **31**, 571–598 (2001).
- <sup>48</sup>B. L. Henke, E. M. Gullikson, and J. C. Davis, "X-ray interactions: Photoabsorption, scattering, transmission, and reflection at  $E = 50\text{--}30\,000\text{eV}$ ,  $z = 1\text{--}92$ ," *At. Data Nucl. Data Tables* **54**, 181–342 (1993).
- <sup>49</sup>M. Koenig, T. Michel, R. Yurchak, C. Michaut, B. Albertazzi, S. Laffite, E. Falize, L. Van Box Som, Y. Sakawa, and T. Sano, "Interaction of a highly radiative shock with a solid obstacle," *Phys. Plasmas* **24**, 082707 (2017).
- <sup>50</sup>J. J. MacFarlane, I. E. Golovkin, and P. R. Woodruff, "Helios-CR a 1D radiation-magnetohydrodynamics code with inline atomic kinetics modeling," *J. Quant. Spectrosc. Radiat. Transfer* **99**, 381–397 (2006).
- <sup>51</sup>F. Ogando and P. Velarde, "Development of a radiation transport fluid dynamic code under AMR scheme," *J. Quant. Spectrosc. Radiat. Transfer* **71**, 541–550 (2001).
- <sup>52</sup>D. García-Senz, P. Velarde, F. Suzuki-Vidal, C. Stehlé, M. Cotel, D. Portillo, T. Plewa, and A. Pak, "Interaction of hemispherical blast waves with inhomogeneous spheres: Probing the collision of a supernova ejecta with a nearby companion star in the laboratory," *Astrophys. J.* **871**, 177 (2019).
- <sup>53</sup>M. Cotel, P. Velarde, C. de la Varga, and A. G. García-Fernández, "Equation of state for laboratory astrophysics applications," *Astrophys. Space Sci.* **336**, 53–59 (2011).
- <sup>54</sup>A. de la Varga, P. Velarde, M. Cotel, F. de Gaufridy, and P. Zeitoun, "Radiative properties for warm and hot dense matter," *High Energy Density Phys.* **7**, 163–168 (2011).
- <sup>55</sup>A. Penzo and J. Tassar, "Establishment of a supercritical shock-wave in the piston problem," *J. Mec. Theor. Appl.* **3**, 381–396 (1984).
- <sup>56</sup>PrismSPECT, <https://www.prism-cs.com/Software/PrismSPECT/overview.html>.
- <sup>57</sup>L. Ibgui, I. Hubeny, T. Lanz, C. Stehlé, M. González, and J. Chièze, "3D spectral radiative transfer with IRIS: Application to the simulation of laboratory models of accretion shocks in young stellar objects," in *Numerical Modeling of Space Plasma Flows (ASTRONUM2012)*, Vol. 474, p. 66, available at: <https://aspl-books.org/custom/publications/paper/474-0066.html>.
- <sup>58</sup>N. Yamaguchi, J. Katoh, Y. Sato, T. Aota, A. Mase, and T. Tamano, "Space-resolving flat-field vacuum ultraviolet spectrograph for plasma diagnostics," *Rev. Sci. Instrum.* **65**, 3408–3414 (1994).
- <sup>59</sup>T. Harada, H. Sakuma, Y. Ikawa, T. Watanabe, and T. Kita, "Design of high-resolution XUV imaging spectrometer using spherical varied line-space grating," in *X-Ray and EUV/FUV Spectroscopy and Polarimetry (SPIE, 1995)*, Vol. 2517, pp. 107–115.
- <sup>60</sup>L. Lecherbourg, "Spectroscopie d'absorption ultra-rapide de rayonnement X pour l'étude de la matière en régime transitoire," Ph.D. thesis, Ecole Polytechnique X, 2007.
- <sup>61</sup>A. Kramida, Y. Ralchenko, J. Reader, and N. A. Team, *NIST Atomic Spectra Database (version 5.8)*, National Institute of Standards and Technology, Gaithersburg, MD, USA, 2020.
- <sup>62</sup>E. B. Saloman, "Energy levels and observed spectral lines of ionized argon ARII through ARXVIII," *Astrophys. J.* **39**, 033101 (2010).